UNIVERSITÀ DEGLI STUDI DI PADOVA

Dipartimento di Fisica e Astronomia "Galileo Galilei"

Master Degree in Astrophysics and Cosmology

Master Thesis

"Dust Extinction of the Stellar Continua in High Redshift Galaxies ($2 \lesssim z \lesssim 7$): the Ultraviolet and Optical Extinction Law"

Thesis Supervisor

Prof.ssa Giulia Rodighiero

Student

Gaia Edes Esposito

Thesis Co-supervisors

Prof. Paolo Cassata

Academic Year 2024/2025

Abstract

Dust in galaxies absorbs a substantial fraction —often exceeding half— of the stellar energy emitted at the ultraviolet and optical wavelengths, significantly impacting our interpretation of galaxy evolution. Accurately quantifying dust obscuration, particularly in galaxies at intermediate to high redshifts, remains a major challenge, introducing considerable uncertainties in the derivation of key physical parameters such as star formation rates, stellar ages, luminosity functions, and more.
However, recent observations, such as those from JWST, are increasing the number of spectroscopically confirmed high-redshift galaxies, enabling more detailed studies of dust attenuation. The aim of this work is to derive the dust attenuation curve for star-forming galaxies at high redshift.

We make use of the JADES Data Release 3 and the ASTRODEEP photometric catalog from JWST. The selected sample consists of ~ 100 star-forming galaxies with stellar masses in the range $9 \lesssim \log(M_*/M_\odot) \lesssim 11$, spanning redshifts $2 \lesssim z \lesssim 7$.

Following the method of Calzetti et al. (1994), we characterize the dust attenuation using the UV power-law index, β, and the Balmer optical depth, $\tau_B^l = \tau_{H\beta} - \tau_{H\alpha}$.
The UV slope is derived by interpolating photometric bands, while the Balmer optical depth is estimated from fully resolved $H\alpha$ and $H\beta$ emission lines, obtained using medium-resolution gratings.
We investigate the $\beta - \tau_B^l$ relation for the entire sample, and subsequently divide the sample into stellar mass bins, focusing on galaxies with $\log(M_*/M_\odot) \geq 9$ —a range where dust absorption is expected to be significant. The sample was then further divided into bins of τ_B^l, and, using low-dispersion prism spectra —particularly suited for studying continuum features— we constructed average spectral templates for each bin. Finally, we derived a selective attenuation curve, $Q(\lambda)$, over the wavelength range $1500\text{Å} < \lambda < 11400\text{Å}$.

The obtained selective attenuation curve is in agreement with findings at $1 \lesssim z \lesssim 2$ by Reddy et al. (2015), Shivaei et al. (2020) and Battisti et al. (2022), and in tension with the recent claims of strong evolution over $2 < z < 11$ by Markov et al. (2024), which are based on modeling assumptions.

Contents

List of Figures

List of Tables

List of Acronyms

AGN Active Galactic Nuclei

API Application Programming Interface

BCGs Blue Compact Galaxies

BLR Broad Line Region

FUV Far-Ultraviolet

GE Galactic Extinction

HST Hubble Space Telescope

IGM Intergalactic Medium

IMF Initial Mass Function

ISM Interstellar Medium

JADES JWST Advanced Deep Extragalactic Survey

JWST James Webb Space Telescope

LMC Large Magellanic Cloud

LOS Line of Sight

MCMC Markov Chain Monte Carlo

MW Milky Way

NLR Narrow Line Region

NUV Near-Ultraviolet

PAHs Polycyclic Aromatic Hydrocarbons

SED Spectral Energy Distribution

SFG Star Formin Galaxy

SFH Star Formation History

SFR Star Formation Rate

SMC Small Magellanic Cloud

SNeII Type II Supernovae

SPS Stellar Population Synthesis

SSP Simple Stellar Population

sSFR specific Star Formation Rate

UV Ultraviolet

WR Wolf-Rayet (stars)

Chapter 1

Introduction

One of the main challenges in observational cosmology over the past several decades has been quantifying the dust opacity of galaxies, across all types and redshifts as a function of wavelength. Addressing this complex issue has required the collective effort of numerous researchers worldwide and, in many respects, it remains open and unresolved problem.

The strong interest in addressing this issue arises from the crucial role of dust in shaping galaxy spectral energy distributions (SEDs) making it difficult to interpret the fundamental properties of galaxies and limiting our understanding of their evolution.

Dust affects observations in two primary ways: by attenuating light in the UV-to-NIR wavelength range—through absorption and scattering of stellar and nebular emission—and by re-emitting the absorbed energy in the infrared, in accordance with energy conservation. To first order, the effect depends on the grain-size distribution[1]: since small grains are more abundant than large ones, shorter wavelengths are more affected, resulting in a reddening of the SED (Iyer et al., 2025).

These effects are particularly impactful in the wavelength ranges where most of observations are conducted. As a result, the interpretation of galaxies SED in terms of key physical parameters —such as age, stellar population mix, star formation rate (SFR), and initial mass function (IMF)— is significantly compromised (Calzetti, 2001).

[1]Dust grains typically range from 5 to 250 nm in size, much smaller than what we commonly refer to as dust on Earth.

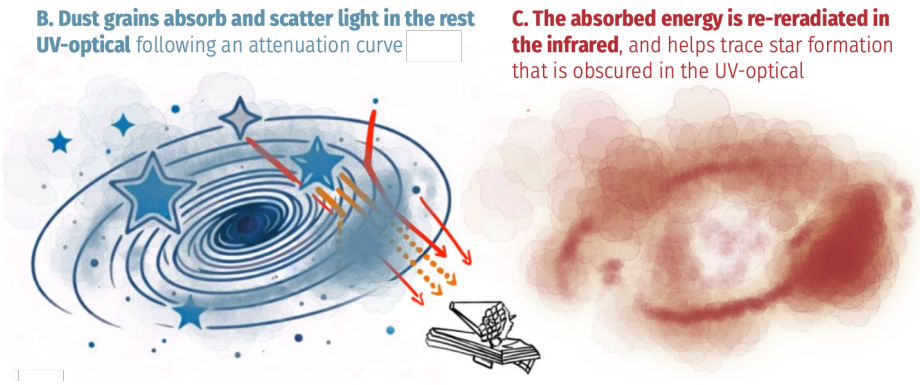

Figure 1.1: A schematic showing dust attenuation in the optical-UV and re-emission in the infrared, Iyer et al. (2025).

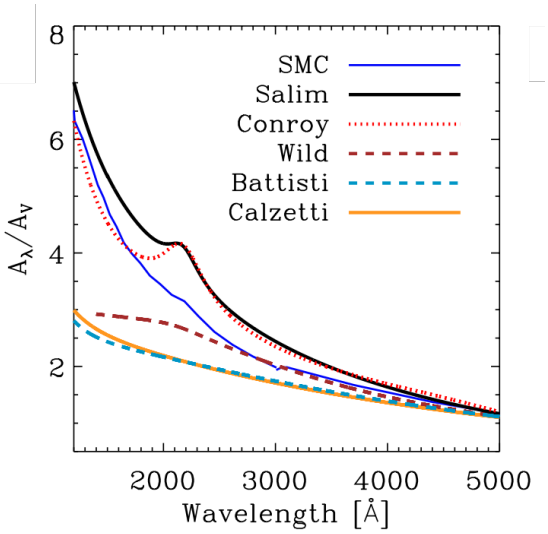

Figure 1.2: Observational characteristics of attenuation curves in the local Universe, Salim and Narayanan (2020).

This interest also stems from the fact that investigating dust extinction in extragalactic systems provides critical insight into the physical processes governing the evolution of grain sizes distribution and compositions across a wide range of galactic environments.
A key focus in high-redshift studies of the extinction curve has been the potential variation of the 2175Å UV bump, a feature typically associated with small carbonaceous grains, including polycyclic aromatic hydrocarbons (PAHs). High-redshift galaxies serve as valuable laboratories for investigating the strength of this feature due to their diverse metallicities (Z) and incident radiation fields (Salim and Narayanan (2020)). Some examples of dust attenuation curves A_λ/A_V, with and without the UV bump, are shown in Figure 1.2.

Moreover, uncertainties in extinction corrections and photometric redshifts of individual galaxies represent a major limitation to the precision of current dark energy studies, affecting the accuracy of both weak lensing and supernova observations (Battisti et al., 2016).

Since young stellar populations are, on average, located in denser dusty clouds than older ones, variations in dust opacity within a galaxy affect the derivation of its star formation history (SFH), by biasing the relative contributions of different stellar age populations.
This introduces the well-known age–dust degeneracy, whereby a galaxy can appear red either because it is genuinely old or because it is heavily obscured by dust. In such cases, dust can cause a galaxy to appear "redder" than it truly is, mimicking the color signature of an older stellar population (Calzetti (2001)).
As a result, dust extinction may cause an underestimation of the contribution from young stars and an overestimation of older populations in SFH reconstructions. This misrepresentation, in turn, affects IMF estimates and complicates efforts to determine whether and how the IMF varies across different environments, such as quiescent or dust-rich galaxies.

Disentangling the effects of age and dust is therefore a non-trivial task and represents one of the main challenges in modern galaxy modeling (Calzetti (2001)).
Past studies (Calzetti et al., 1994; Calzetti, 2001) have primarily focused on starburst galaxies and blue compact galaxies (BCGs), as these populations are characterized by intense episodes of star formation, making them ideal laboratories for investigating the effects of dust on stellar light. Other studies have targeted star-forming galaxies (SFGs) more broadly,

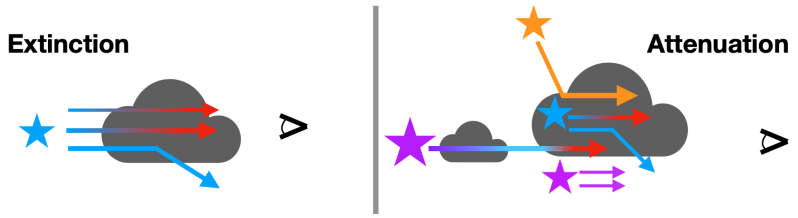

Figure 1.3: Schematic summarizing the difference between extinction and attenuation. The former encapsulates absorption and scattering out of the line of sight, while the latter folds in the complexities of star-dust geometry in galaxies, and may include scattering back into the line of sight, varying column densities/optical depths, and the contribution by unobscured stars, Salim and Narayanan (2020)

given their crucial role in shaping our understanding of the star formation history and the overall evolution of galaxies (Battisti et al., 2016).
However, due to the limited availability of multi-wavelength observations, most of these studies have been confined to the local Universe, where data are more accessible and reliable.

The well-known Calzetti dust attenuation law (Calzetti et al. (1994), Battisti et al. (2016)) has been widely applied to correct for reddening in galaxies of various types across a broad range of redshifts. It is therefore essential to evaluate whether this law is truly universal and can be reliably extended to galaxies with different physical properties and at different cosmic epochs.

In recent years, several studies have aimed to explore the evolution of dust attenuation with redshift, including works by Reddy et al. (2015), Shivaei et al. (2020), Battisti et al. (2022), Markov et al. (2024), and Markov et al. (2025)—see Section 1.3.

Historically, the absolute value and wavelength dependence of the dust extinction curve have been determined by comparing reddened and unreddened stars. This corresponds to a simple dust-to-star geometry: it is straightforward to assume a point-like background source with a uniform foreground dust screen. In this configuration, the absorption and scattering of photons by dust grains both contribute to removing flux from the line of sight (LOS). This loss of light is referred to as *dust extinction*, and it depends solely on the intrinsic properties of the dust.

However, for extended regions or sources, like galaxies, the assumption of a foreground extinction screen becomes insufficient. In more complex geometries, the scattering of photons—while still responsible for removing light from the original path—can also redirect some photons back into the line of sight, like showed in the simple sketch in Figure 1.3. We refer to *dust attenuation* when the dusty medium is not arranged as a simple foreground screen, but is instead mixed with the stars in a more complex spatial configuration. This results in a weaker net dimming of the observed light compared to a simple screen geometry. If we adopt the historical extinction law, we may overestimate the overall correction (Calzetti et al. (1994), Markov et al. (2024)).

Hence, in conclusion, the fundamental difference between reconstructing the extinction curve in nearby galaxies, like Milky Way or Magellanic Clouds, and high-redshift galaxies is that in the first case dust extinction can be directly measured using individual stars, so that the size distribution and composition of dust grains are directly related to the observed extinction. In the latter, we are forced to use unresolved stellar populations, which have more complicated

SEDs as a result of being composed of many stars of different stellar populations and will depend on the SFH and IMF. Ultimately, using collections of stars rather than individual stars introduces the additional factor of geometry, further complicating the overall picture of extinction (Battisti et al. (2016)).

It is therefore important to note that attenuation is not a direct measure of dust properties. Rather, it is a combination of extinction, geometry, and scattering effects that collectively influence the observed SED of galaxies.

As explained by Calzetti et al. (1994), the difficulty in defining a consistent model for dust attenuation in extended regions, such as galaxies, lies in two main aspects:

(a) the emerging flux depends on the *geometrical distribution* of dust inside the region;

(b) the *composition* and *grain size distribution* of dust in the ISM are not well determined;

Both factors influence the shape of the dust attenuation curve in galaxies. Regarding the *geometrical distribution* of dust with respect to stars, dust can be intermixed with gas—and therefore with stellar light sources—within the interstellar medium (referred to as internal dust), and can be concentrated in clumpy structures such as molecular clouds, dense HII regions, filaments and spiral arms of galaxies. If dust is strongly clumped, some LOS can be heavily attenuated while others remain nearly transparent. This creates a net effect of *gray attenuation*[2], as ultraviolet (UV) light can escape through less dense regions, reducing the observed optical depths at short wavelengths. As the dust-to-star geometry becomes increasingly complex, the attenuation curve tends to flatten and the characteristic UV bump at 2175Å weakens in prominence, regardless of the intrinsic dust extinction curve. On the other side, simpler geometries that more uniformly obscure UV light produce steeper attenuation curves.

In addition to dust geometry, the *grain size distribution* influences the differential absorption behavior and, consequently, the shape —particularly the slope— of the dust attenuation curve. A more uniform distribution of grain sizes leads to grayer attenuation. As a result, even in the presence of significant dust, color variations remain small. The *composition* of the dust, which is closely tied to the galaxy's metallicity, affects both the overall slope of the attenuation curve from the near- to far-UV and the prominence of the 2175Å UV bump.

Beyond complex dust-to-star geometries and grain properties, one of the main drivers of dust attenuation variation in shape (and normalization) is the V-band attenuation (A_V). This trend is probably a manifestation of a more fundamental dependence on the dust column density along the LOS, for which the optical attenuation serves as a proxy.
Larger A_V values correspond to flatter attenuation curves: such correlation has been confirmed both theoretically and observationally. Physically, in the low-A_V (optically thin) regime, UV photons are more likely to be scattered and eventually absorbed, steepening the attenuation curve. Conversely, in the high-A_V (optically thick) regime, the curve appears flatter due to a combination of scattering back into the line of sight and the contribution of unobscured OB stars (Salim and Narayanan (2020), Markov et al. (2024)).
Of course, this effect depends on the inclination of galaxies. Splitting the sample by inclination, Battisti et al. (2017) did find a correlation with the attenuation curve slopes, such that highly inclined galaxies have shallower slopes with a possible weak bump, whereas face

[2]Meaning that the curve becomes flatter, i.e. light absorption becomes less dependent on wavelength compared to a typical extinction curve.

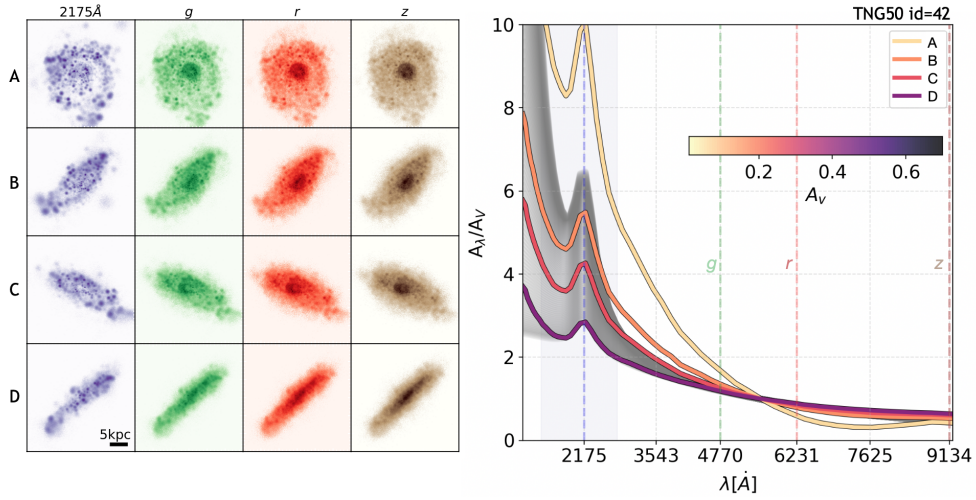

Figure 1.4: Left Panel: Images of a TNG50 galaxy (id 42) observed along different lines of sight, with increasing values of visual attenuation (A_V) from top to bottom. Each row shows the predicted emission at a different wavelength: 2175 $\AA$, and the SDSS g, r, and z bands. Right panel: Corresponding attenuation curves for each line of sight, color-coded according to A_V (see colorbar), Sommovigo et al. (2025).

on galaxies had steeper slopes. The strength of the UV bump was found to be stronger in edge-on galaxies. Simulations by Sommovigo et al. (2025) using the TNG50 galaxy sample illustrate the effect of inclination on the visual attenuation A_V and on the shape of the attenuation curve, as shown in Figure 1.4.

In turn, these main drivers depends on galaxy properties, like the metallicity (Z) and the environmental UV radiation. Since A_V reflects the dust column density, it is shaped by the total dust content of a galaxy, which scales with both its metallicity, Z, and gas mass M_{gas}. In general:

$$M_{dust} \propto Z \cdot M_{gas} \tag{1.1}$$

Dust formation is primarily regulated by asymptotic giant branch (AGB) stars, core-collapse supernovae (SNII), and subsequent grain growth via accretion in the interstellar medium (ISM). The raw materials for dust—heavy elements such as carbon, silicon, and iron—are produced by stars during their lifecycles. However, the presence of gas is also essential for the formation and survival of dust. In particular, for dust to condense and grow efficiently through ISM accretion, gas must be present at low temperatures and with sufficient density. Conversely, dust grains can be destroyed by energetic events such as supernova shocks (Rémy-Ruyer et al. (2014), Inoue (2011)).

As the galaxy evolves, the gas content decreases as it is consumed in star formation, while the metallicity increases because stars process gas into heavy elements, which are then returned to the ISM through stellar winds and supernovae. Since the trends of Z and M_{gas} move in opposite directions, we expect that the dust content reaches a peak during the galaxy's evolution (Calzetti et al. (1994)).

Several studies comparing the Milky Way (MW), Large Magellanic Cloud (LMC), Small Magellanic Cloud (SMC) extinction laws, show that they have different trends as a function of the wavelength for $\lambda \lesssim 2600$Å: the slope increases and the UV bump decreases in strength going from the MW, to the LMC, to the SMC. This discrepancy is thought to stem from differences in the metallicity of the three galaxies.

Mid- and far-infrared studies of star-forming regions in the MW have shown that the environmental UV radiation intensity appear to play as important role as the metallicity in shaping the extinction curve: the UV energy density level affects the grain size distribution, via deconstruction or coagulation, and the dust physical characteristics, via ionization state changes (Calzetti (2001)).

Therefore, even if high-redshift galaxies, on average, have lower metal content, this does not necessarily imply a lower dust content. In fact, young galaxies can exhibit significant amounts of dust despite their early evolutionary stage as they still retain large gas reservoirs, which facilitate efficient dust growth in the ISM, in addition to the dust initially produced by massive stars. Moreover, dust formation in distant galaxies may occur rapidly due to the presence of type II supernovae (SNeII) or Wolf-Rayet (WR) stars, which are efficient producers of heavy elements. Thus, high gas mass (M_{gas}) can compensate for low metallicity (Z), allowing for substantial dust content even in metal-poor environments.

A key issue that has emerged in high-redshift studies is the quantification of the differential attenuation between ionized regions and the stellar continuum.
Calzetti et al. (1994) reported that nebular lines in galaxies experience significantly greater attenuation than the stellar continuum. They determined a typical ratio of color excess, E(B–V), between nebular and stellar region. In particular, the difference in optical depth between the Balmer emission lines Hα and Hβ is ~ 2 times larger than the difference in the optical depth between the continuum underlying the two Balmer lines. This result was interpreted as a consequence of the fact that the hot ionizing stars are associated with dustier regions than the cold stellar population is. Evidence for increased attenuation toward nebular regions may indicate the presence of a birthcloud-like dust component introduced by Charlot and Fall (2000).
These results were confirmed for low-redshift galaxies in the large-scale study by Wild et al. (2011), but evidence for the need for additional attenuation toward HII regions at high redshift remains inconsistent (see Section 1.1.4).

Despite decades of study, several key questions about dust attenuation and its role in galaxy evolution remain unresolved:

1. What are the potential drivers of attenuation curve slope differences beyond the optical opacity that can be probed observationally? How much of the scatter is due to the different intrinsic extinction curves? How do we test this?

2. What drives the evolution of the grain size distribution in galaxies across the mass function over cosmic time?

3. What is the minimum number of independent parameters necessary to develop a parameterization for attenuation curves that captures the diversity of effective attenuation curves across different spectral regimes?

It's strictly important to constrain the attenuation curve as a function of galaxies properties, and to identify the main drivers of the evolution of the attenuation curve across cosmic time, in order to obtain a clear picture of galaxy evolution.

1.1 Theory and Modeling: Basic Concepts

The interstellar medium of galaxies consists of a multiphase mixture of gas, plasma, and dust grains, which serve as the primary reservoirs of star formation fuel and are in turn in-

fluenced by feedback from both stars and Active Galactic Nuclei (AGN) (Iyer et al. (2025)). The gaseous component of galaxies —including both atomic and molecular phases— contributes to their SEDs through a variety of emission mechanisms, such as collisionally excited and auroral lines, as well as rotovibrational and spin-flip transitions. These features are commonly grouped under the term "nebular emission", which refers to nebulae of ionized gases surrounding young star, where such emissions are produced. The nebular emission of galaxies is influenced by the chemical abundance and composition of the gas, the intensity of the ionizing radiation field, and the gas-to-dust ratio.

The ISM gas of galaxies is composed by:

- **Molecular gas - H_2**: Molecular gas, which is cold and dense and primarily composed of H_2, serves as the main reservoir for star formation. CO molecules, commonly used as tracers of this phase, are excited through collisions with H_2 and emit via low-energy rotational transitions detectable at radio wavelengths.
- **Atomic gas - HI**: Atomic gas, composed mainly of neutral hydrogen (HI), acts as a reservoir of material that cools and is converted into (H_2), to form stars. In diffuse interstellar clouds, HI tends to be cool in the inner regions and warmer in the outer layers, where it can become partially ionized by the hard ultraviolet photons of the interstellar radiation field. HI emits at a wavelength of 21-cm, which corresponds to the spin-flip transition between the two hyperfine levels of the fundamental state.
- **Ionized gas - HII**: Ionized gas exists both as diffuse intercloud material and as concentrated HII regions. The diffuse component is characterized by high temperatures but extremely low densities. According to the model proposed by McKee and Ostriker (1977), the state of the ISM is largely governed by supernova explosions, which sweep up gas, disrupt molecular clouds, and sustain the hot, ionized intercloud medium. When molecular gas cools and star formation occurs, the newly formed O- and B-type stars emit large numbers of ionizing photons that irradiate the surrounding birth cloud, creating an HII region. These regions are easily detectable through strong hydrogen and oxygen emission lines in the optical spectrum.

The spectrum of an HII region is characterized by strong emission lines and a continuum component, coming from two sources: recombination processes and the radiative cooling of collisionally excited gas.
The **continuum** consists of free–free (Bremsstrahlung radiation resulting from electron-ion interactions), free-bound (arising from radiative recombination events), and two-photon emission (from the decay of the metastable $2^2S_{1/2}$ state of Hydrogen). This emission is the strongest at high ionization parameters U[3] and low metallicities Z. It is especially prominent near the Balmer break ($\sim$ 3646Å) in local young star clusters or in high redshift galaxies that are still in low Z environment.

The **emission-line** component is the result of recombination of ions and radiative de-excitation of collisionally excited molecules, atoms, and ions in the gas cloud (Osterbrock and Ferland (2006); Kewley et al. (2019)). If the cloud is optically thin, all photons issued from recombination can escape the nebula (case-A recombination). Otherwise, all photons issued from recombination that cascade to the ground state are immediately reabsorbed by a neutral hydrogen atom, so that all downward transitions to the n=1 level can be ignored (case-B recombination, more common in astrophysical contexts). In this case, every

[3]defined as the ratio of ionizing photon density to hydrogen density.

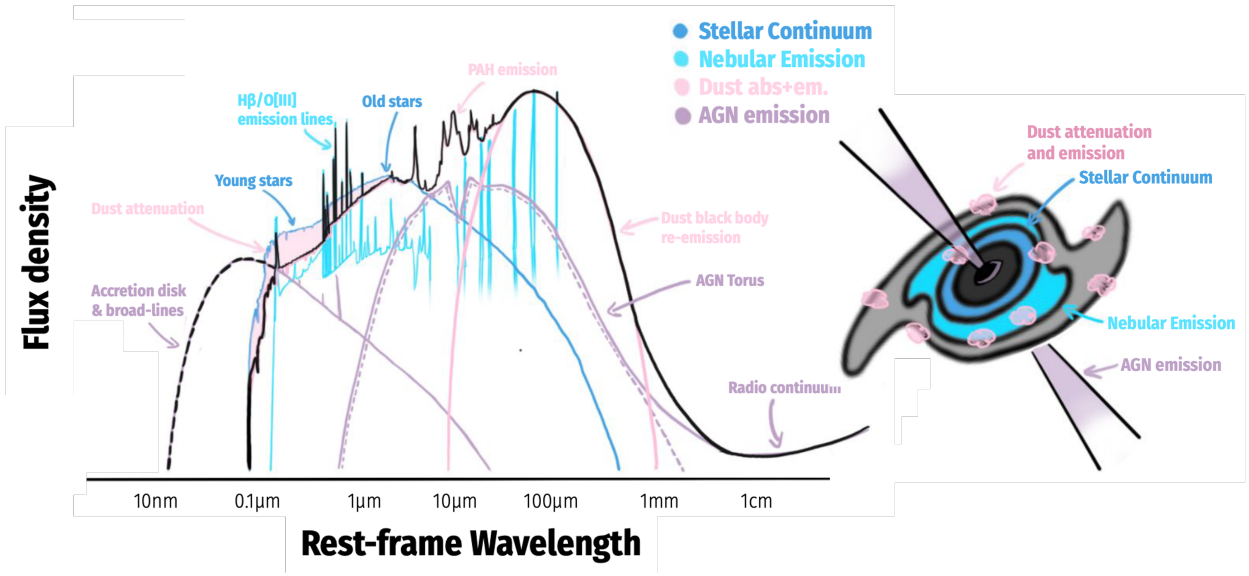

Figure 1.5: A schematic of a galaxy's pan-chromatic SED, broken down by source of emission at different wavelengths, Iyer et al. (2025).

recombination must eventually yield a Balmer photon (transition to the n=2 level) at optical wavelengths.

1.1.1 Extinction Law Theory: Basic Framework

Cosmic dust particles (or grains) form in the atmospheres of evolved stars, such as AGB stars, and are released into the ISM by stellar winds or explosions (**?**). Dust grains typically range in size from 5 to 250 nm, with the composition being carbonaceous and silicate depending on whether the stars are carbon- or oxygen-rich respectively.

The optical depth seen by photons interacting with dust is:

$$\tau_{\rm dust}(\lambda) = \mathrm{N_d} \cdot \mathrm{Q_{ext}} \cdot \pi \cdot a^2 \tag{1.2}$$

where $\mathrm{N_d}$ is the column density of dust, a is the size of the grain (therefore assuming a spherical geometry) and $\mathrm{Q_{ext}}$ is the ratio of the extinction cross section to the geometric cross section (Salim and Narayanan (2020)). The extinction cross section is the sum of the absorption and scattering cross sections, and depends on the grain composition (**?**). In order to develop a theoretical model for the extinction law, one must therefore simultaneously develop a model for the size distribution (a), as well as for the composition of the interstellar grains.

Dust is heated by short wavelength photons and re-emits light at long wavelengths. About half of all the UV/optical light produced by stars in the Universe is reprocessed by dust (Dole, H. et al. (2006)).

Factors such as the amount of dust surrounding the birth-clouds of young stars, grain-size distributions, the ratio of silicates and carbonate grains, the clumpiness of dust in the ISM, and even galaxy-wide factors like the inclination of galaxies with respect to the observer can affect the amount of differential attenuation affecting the stellar populations in any given galaxy.
Dust emission can be represented as a combination of out-of-equilibrium PAHs heated in

the photodissociation regions around young stars (Li and Draine (2001)) and black body emissions at different temperatures in the mid- to far-IR (da Cunha et al. (2008)). The far-IR emission is characterized by a bump that depends on the temperature of warm and cold grains in thermal equilibrium.

Some attenuation curves feature a "dust bump" in the UV around $\sim$ 2175Å due to PAHs and other small grains (Noll et al. (2009); Kriek and Conroy (2013)). The existence of the 2175Å extinction bump points to at least some carbonaceous grains in the ISM (Salim and Narayanan (2020)). It's debated if the presence of the 2175Å is rare, or sometimes simply not visible. According to Calzetti et al. (1994), the absence of the 2175Å dust feature can be due either to the effects of the scattering and clumpiness of the dust, or to a chemical composition different from that of MW dust grains. Disentangling the two interpretations is not easy because of the complexity of the spatial distribution of the emitting regions.

In general, all models deriving attenuation laws share the same basic methodology:

1. they develop a model for the structure of galaxies and populate them with stars and ISM;
2. they make assumptions regarding the extinction properties of the dust grains in those galaxies;
3. they model the radiative transfer of stellar light as it escapes these systems.

The major difference between models lies in how the star-dust geometry is specified. Simulation methods range from relatively simplified analytic prescriptions for galaxy structure to complex hydrodynamic galaxy formation simulations. More complex simulations likely reflect a more realistic star-dust geometry, though at the expense of both increased computation time and ease in isolating the impact of individual physical phenomena on the final dust attenuation curve.
The structure of the ISM in analytic models can range from simple screen models (e.g., Calzetti (2001)) to models that include stellar birthclouds (e.g., Charlot and Fall (2000), Wild et al. (2011)).

1.1.2 Radiative Transfer Equation

The configuration of the relative distribution of ionized gas and dust, namely the star-dust geometry, plays an important role in shaping the attenuation curve. According to the model involved for the relative distribution, the equation of the radiative transfer has different solutions (Calzetti et al. (1994)).
In the plane parallel approximation of slab of dust and ionized gas, the radiative transfer equation can be written as:

$$\cos\theta \frac{\partial I_\lambda}{\partial z} = -k_\lambda I_\lambda + \epsilon_\lambda + k_\lambda \frac{\omega_\lambda}{4\pi} \int I_\lambda \Phi(\cos\Theta) d\Omega \tag{1.3}$$

where θ is the angle between the direction perpendicular to the plane and the direction of the light beam; I_λ is the radiation intensity; k_λ is the extinction coefficient of the dust, given by the sum of the absorption and the scattering coefficients; ϵ_λ is the emissivity of the sources embedded in the slab; ω_λ is the albedo, which is the probability of a photon to be scattered; $\Phi(\cos\Theta)$ is the phase function of the dust grains, which is the probability of a photon to be scattered in a certain direction, depending on Θ which is the angle between

the directions of the incident and scattered photon.

The three terms on the right-hand side of equation 1.3 represent respectively: the loss of intensity of the beam due to absorption and scattering; the contribution to the emerging flux due to the sources in the slab; the positive contribution to the intensity due to scattering of the light back into the beam. The dust emissivity term has been neglected, since it becomes important in the infrared, while we are interested in the attenuation in the optical and UV wavelength regions.

Five models can be considered to represent different configurations of the relative distribution of ionized gas and dust, as shown in Figure 1.6:

1. *Uniform dust screen*: This configuration is commonly applied when dereddening individual stars. The screen is physically distant from the cloud of ionized stars, so the effect of dust grains is to remove photons from the LOS through absorption and scattering. This model can be an over-simplification in the case of galaxies;
2. *Clumpy dust screen*: The dust is located in a screen distant from the cloud of gas, but in this case the dust is organized in clumps. This model is more realistic than model 1;
3. *Uniform scattering slab*: The slab is close to the source of radiation, implying that the action of scattering by grains is also to convey photons back into the LOS, giving a positive contribution to the emerging radiation;
4. *Clumpy scattering slab*: Similar to model 3, but dust is clumped;
5. *Internal dust*: Dust and ionized gas are uniformly mixes.

Here, we briefly summarize the solution of equation 1.3 for each model.
– In *model 1* the dust screen is detached from the cloud of ionizing gas, which means $\epsilon_\lambda = 0$, as well as the third term on the right-hand side of the equation is zero. The solution for the emerging radiation is therefore:

$$I_\lambda = I_\lambda^0 e^{-\tau(\lambda)} \tag{1.4}$$

with extinction optical depth:

$$\tau(\lambda) = k_\lambda z/\cos\theta.$$

– In *model 2* the second and third terms on the right-hand side of the equation are still zero, so the form of the solution remains the same as in equation 1.4, but with an effective optical depth $\tau_{\mathit{eff}}(\lambda)$. An analytical solution can be found by assuming that all clumps have the same optical depth and are Poisson-distributed, with an average number $\mathcal{N}$ of clumps along the LOS. The average optical depth $\tau_m(\lambda)$ —i.e., a measure of the total dust content in front of the emitting region— is given by: is $\tau_m(\lambda) = \mathcal{N}\tau_c(\lambda)$. However, in an inhomogeneous configuration, $\tau_m(\lambda)$ does not coincide with the effective optical depth $\tau_{\mathit{eff}}(\lambda)$, which quantifies the actual attenuation experienced by the emerging radiation. In this case, the effective depth is given by:

$$\tau_{\mathit{eff}}(\lambda) = \mathcal{N}[1 - e^{-\tau_c(\lambda)}] \tag{1.5}$$

The general solution for the intensity is therefore:

$$I_\lambda = I_\lambda^0 e^{-\tau_{\mathit{eff}}(\lambda)} = I_\lambda^0 e^{-\mathcal{N}(1-e^{-\tau_c})} \tag{1.6}$$

In the asymptotic case $\tau_c \ll 1$, the behavior of the clumpy dust screen becomes observationally indistinguishable from that of a uniform dust screen, since $\tau_{\mathit{eff}}(\lambda) \approx \tau_m(\lambda)$. Conversely, in the limit $\tau_c \gg 1$, the flux saturates because the opacity itself becomes saturated: further increases in dust content, and hence in $\tau_c(\lambda)$, do not result in a corresponding increase in $\tau_{\mathit{eff}}(\lambda)$. It is important to note that, for large $\mathcal{N}$, the clumpy model reproduces the behavior of a uniform screen regardless of the value of τ_c, making the two models observationally indistinguishable.

– In *model 3*, in contrast to model 1, scattering provides a positive contribution to the emerging radiation, making the integral in the equation non-zero. Thus, the result depends on the albedo ω_λ and the phase function $\Phi(\cos\Theta)$. It can be approximated by considering the two extreme cases: the isotropic scattering, with $\Phi(\cos\Theta) = 1$, and the forward-only scattering, with $\Phi(\cos\Theta) = 2\delta(\cos\Theta - 1)$. The intermediate cases can be approximated introducing a weight parameter h_λ describing the anisotropy of the scattering, such that:

$$\Phi(\cos\Theta) = h_\lambda + (1 - h_\lambda)2\delta(1 - \cos\Theta) \tag{1.7}$$

In this way, the solution of the equation can be written as:

$$I_\lambda = I^0_\lambda e^{-\tau_{sc}(\lambda)} \tag{1.8}$$

with:

$$\tau_{sc}(\lambda) = a_{\mathit{eff}}(\lambda)\tau(\lambda) \tag{1.9}$$

where:

$$a_{\mathit{eff}}(\lambda) = h_\lambda\sqrt{1 - \omega_\lambda} + (1 - h_\lambda)(1 - \omega_\lambda) \tag{1.10}$$

– *Model 4* includes the properties of both models 2 and 3. Dust is organized in clumps, so τ_{eff} is given by equation 1.5. But now $\tau_m(\lambda) = \tau_{sc}(\lambda)$ given by 1.9, such that:

$$\tau_c(\lambda) = \frac{\tau_{sc}(\lambda)}{\mathcal{N}} \tag{1.11}$$

– In *model 5*, the radiation sources are uniformly mixed with the gas; therefore, the emissivity is constant, $\epsilon_\lambda = \text{const}$. Scattering effectively redirects photons along the line of sight, and this effect can be approximated using equations 1.9 and 1.10. A solution of equation 1.3 is:

$$I_\lambda = I^0_\lambda \frac{1 - e^{-\tau_{sc}(\lambda)}}{\tau_{sc}(\lambda)} = I^0_\lambda \gamma(\lambda) \tag{1.12}$$

In this case, the flux can reach saturation if $\tau_{sc} \gg 1$, since $I_\lambda \to I^0_\lambda/\tau_{\mathbf{sc}}$ in the asymptotic limit.

The configuration of dust and stars within a galaxy significantly affects the shape of the attenuation curve. In principle, the radiative transfer equation should be solved for each geometry to model the attenuation. However, full solutions depend on various unknowns (e.g., dust distribution, albedo, scattering phase function), and are not directly applicable to empirical data.
Calzetti et al. (1994) founds the integrated galaxy light is affected in a way that mimics the uniform dust screen model. In such model, the attenuation at each wavelength is proportional to the dust optical depth τ^l_B leading to predictable and linear changes in the

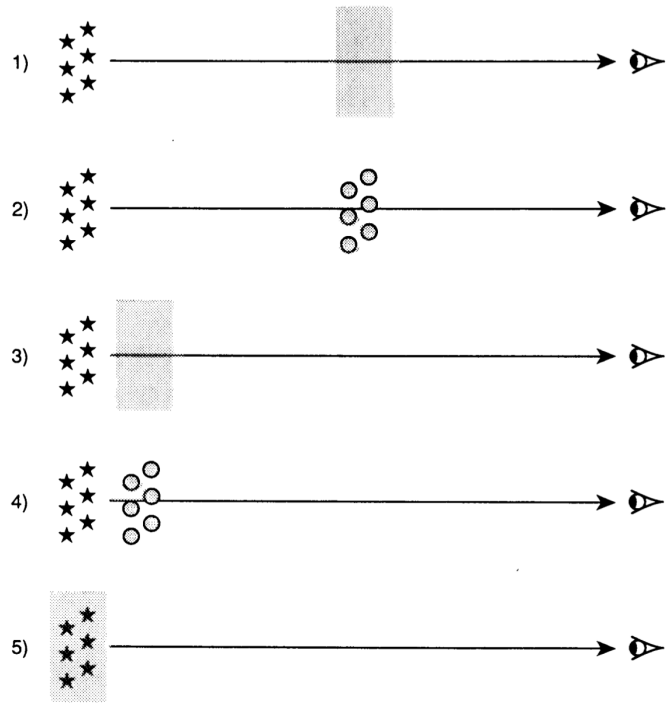

Figure 1.6: A schematic representation of the five configurations of dust/ionized gas. From top to bottom, they are (1) the uniform dust screen; (2) the clumpy dust screen; (3) the uniform scattering slab; (4) the clumpy scattering slab; (5) the internal dust model, (Calzetti et al. (1994)).

shape of the observed spectrum as dust content increases. Specifically, the reddening of the UV continuum —and so, the SED slope quantified by β— increases linearly with optical depth. Similarly, the Balmer decrement —used to compute τ_B^l— increases with the amount of dust affecting ionized gas. The observed relation between β and τ_B^l is linear and thus compatible with a uniform foreground screen (model 1) configuration, in which attenuation is proportional to opacity: $A(\lambda) = 1.086 \cdot \tau(\lambda)$.
In contrast, more complex geometries, such as mixed or clumpy distributions, produce non-linear or saturating relations between the observed flux — and thus attenuation — and the dust content — namely, the optical depth. This leads to a non linear relationship $\beta - \tau_B^l$.

As a consequence, despite the physical complexity of dust geometries in real galaxies, the foreground screen approximation proves effective in capturing the average behavior of the attenuation, and enables the empirical derivation of attenuation curves via quantities like the Balmer optical depth τ_B^l, as addressed in details in Section 1.2.

1.1.3 Definitions of Attenuation Curve

We define *effective extinction* (or attenuation) A_λ, the measure in magnitude of dimming of light suffered by an extended source at the specified band:

$$A_\lambda = m_{\lambda,a} - m_{\lambda,0} \tag{1.13}$$

where $m_{\lambda,0}$ is the magnitude of the dust-free source, and $m_{\lambda,a}$ is the measured (attenuated) magnitude. Equivalently:

$$A(\lambda) = -2.5 \cdot \log_{10}\left(\frac{F_\lambda^a}{F_\lambda^0}\right) \tag{1.14}$$

We call *dust attenuation curve*, the effective extinction A_λ as a function of wavelength. In the literature, dust attenuation curves have been formulated in three different ways, depending on the chosen normalization and whether the curve is absolute or relative (Salim et al. (2018)). They are the selective, total and absolute attenuation curves, defined as follows:

$$\begin{aligned} \text{Selective:} \quad & \frac{A_\lambda - A_V}{A_B - A_V} \\ \text{Total:} \quad & \frac{A_\lambda}{A_B - A_V} \\ \text{Absolute:} \quad & \frac{A_\lambda}{A_V} \end{aligned} \tag{1.15}$$

An higher value of A_λ corresponds to an higher content of dust. The V-band attenuation, A_V, which represents the attenuation at $\lambda = 5500$Å, approximately quantifies the galaxy dust content along the LOS. The V band lies in a wavelength range between the UV and the IR, where extinction is significant but not as dramatic as in the UV, nor as flat as in the IR. This makes it a representative measure of the overall dust effect. Additionally, many stars emit light in the V band, making it an ideal choice for studying large samples of stars and galaxies without too much dependence on spectral type.
Since two galaxies can share the same attenuation law, with one exhibiting a higher A_λ —indicating it is dustier— A_λ must be normalized in order to derive the attenuation curve. This normalization removes the differences due to the total dust content and isolates the shape of the attenuation curve, independent of the absolute amount of dust.
In selective and total formulations, the normalization is done by the color excess $E(B-V) \equiv A_B - A_V$. The total formulation of the attenuation curve is usually denoted as k_λ:

$$k_\lambda = \frac{A_\lambda}{E(B-V)} \tag{1.16}$$

The normalization implies that $k(B) - k(V) \equiv 1$ by definition, so the slope of all total attenuation curves will be equal in the region $B - V$. The value of the total attenuation curve in the V band is $k_V = A_V/E(B-V) \equiv R_V$, and is known as the ratio of total to selective extinction in V. This parameter can be related to the dust grain environment along the LOS, which varies the interstellar extinction: Cardelli et al. (1989) showed that both the steepness of the far-UV ($\lambda \lesssim 0.3\ \mu m$) rise of the extinction curve and the strength of the 0.2175 μm absorption feature decrease for increasing R_V, where low values of R_V correspond to diffuse ISM LOS, while high values associated with dense clouds. The large values of R_V in dense clouds are also consistent with dust grains having systematically larger sizes than in the diffuse medium.
Obviously, this framework becomes more intricate when moving from local galaxies, where individual stars can be resolved, to distant, unresolved systems. In the latter, R_V will also depend on the geometry of dust with respect to stellar populations.

Estimating R_V requires either NIR photometry or total infrared data, so due to the lack of IR data (i.e., the energy balance), the selective formulation is the most common in literature. The selective attenuation curve is related to the total curve as $k_\lambda - R_V$, giving only the relative attenuation with respect to V.

The third formulation, i.e. the absolute attenuation curve, is more intuitive, since it involves the normalization by the absolute attenuation A_V. For historical reasons, the normalization of the curve is tied to the V band, though ideally it should be at longer wavelengths, because different sightlines in our galaxy still show some variations in the extinction curves around V (Cardelli et al. (1989)). This form is related to the total curve formulation through:

$$A_\lambda/A_V = k_\lambda/k_V = k_\lambda/R_V \tag{1.17}$$

This formulation is more intuitive because two curves with the same slopes in the total formulation, but offset from each other due to different R_V values, will not share the same slopes in the absolute formulation. Lower R_V values imply that for the same A_V, the attenuation at B would be higher, resulting in a steeper absolute attenuation curve in the optical range. This suggests that dust affects light in distinct ways.

1.1.4 Differential Attenuation: Nebular vs Stellar Emission

In a galaxy, we distinguish the light coming from the stellar continuum and the nebular emission. The stellar continuum is the light of a galaxy's stars, based on its stellar populations —including the older one— such that the light is shaped by their age and metallicity. The nebular emission is the light coming from collisionally excited gas and plasma in the ISM. It's composed by both nebular continuum and emission lines. Emission lines, such as Hα, arise from HII regions, where gas is ionized by young stars.
If the nebular light is more attenuated, it means that the dust is denser near the young stars.

A key issue that has emerged in high-redshift studies is the quantification of the differential attenuation between ionized regions and the stellar continuum.
The findings of Calzetti et al. (1994) about the differential reddening between nebular emission and stellar continuum, led to the introduction of a two-component model of dust attenuation by Charlot and Fall (2000). In this model, the radiation from all stars is attenuated by a diffuse interstellar medium dust component. However, stars younger than a threshold age $t_{\text{threshold}}$ —approximately 10 Myr, corresponding to the typical dispersal timescale of their birth clouds— experience additional attenuation due to their surrounding natal birthclouds. Both the birthclouds and the ISM attenuate light according to fixed power-law attenuation curves, named *component curves*, to distinguish them from the resulting effective attenuation curves:

$$A_\lambda = \begin{cases} A_{V,\text{ISM}} \left(\frac{\lambda}{\lambda_V}\right)^{-n_{\text{ISM}}} + A_{V,\text{BC}} \left(\frac{\lambda}{\lambda_V}\right)^{-n_{\text{BC}}} & t \leq t_{\text{threshold}} \\ A_{V,\text{ISM}} \left(\frac{\lambda}{\lambda_V}\right)^{-n_{\text{ISM}}} & t > t_{\text{threshold}} \end{cases} \tag{1.18}$$

where n_{BC} and n_{ISM} correspond to power-law exponents for the diffuse ISM and natal birthclouds.
Charlot and Fall (2000) found that a single exponent of $n = 0.7$ for both components worked well for: reproducing the attenuation of nebular lines, and the relation between infrared excess and UV slope (IRX–β relation). da Cunha et al. (2008) later suggested that a steeper exponent, $n = 1.3$, is more appropriate for birthclouds.
The effective attenuation curve resulting from this model becomes steeper following a strong

burst of star formation.
Furthermore, Inoue (2005) showed that because the young luminous stars which dominate at short wavelengths are also the most heavily attenuated, the resulting effective curve will be steeper than the component curves. Moreover, the non-homogeneous distribution, meaning that high-density regions contain young luminous stars, amplifies this effect.

As we previously mentioned, the need for additional attenuation toward HII regions in high redshift galaxies, is highly debated.
Reddy and Steidel (2004), Erb et al. (2006), Reddy et al. (2012), and Shivaei et al. (2015) found that the dust reddening affecting nebular regions is comparable to that of the stellar continuum, based on comparisons of SFR indicators derived from X-ray, UV, Hα, infrared, and radio observations. Meanwhile, Förster Schreiber et al. (2009), Wuyts et al. (2011), Price et al. (2014), report evidence for additional attenuation toward nebular regions, in agreement with the two-component birthcloud model.
An important step forward to clarify this discrepancy was made by Price et al. (2014), who found not only the need for increased attenuation toward HII regions in $z \sim 1.5$ galaxies, but also a decreased difference in A_{HII} compared to A_{UV} with increasing sSFR, later confirmed by Puglisi, A. et al. (2016). The physical interpretation is that a galaxy with a high sSFR is expected to host a large population of OB stars, which reside within optically thick birth clouds. In such cases, these massive stars dominate both the UV continuum and emission lines, resulting in similar levels of attenuation for the continuum and nebular emission. In these situations, $A_{HII} \sim A_{UV}$. Conversely, in galaxies with low sSFR, the number of OB stars is reduced, and the UV-optical continuum is primarily produced by less massive stars located in both the birth clouds and the diffuse interstellar medium (ISM). Here, $A_{HII} > A_{UV}$, as the emission lines originates from regions with higher dust density compared to those contributing to the continuum.
A correlation with sSFR is observed even at low redshift (Wild et al. (2011)), where the ratio of $A_B - A_V$ reddenings for nebular and continuum emission approaches unity in the case of extreme local starbursts.

1.2 Methodology for Characterizing Attenuation

Calzetti et al. (1994) investigated the discrepancy between the dust extinction measured from Balmer line ratios and that inferred from the UV stellar continuum, by analyzing UV and optical spectra of the central regions of 39 line-emitting starburst and blue compact galaxies.

The main difficulty in characterizing dust attenuation in the UV arises from the degeneracy between dust effects and stellar population aging. While in the optical range the Balmer line ratio provides a robust diagnostic of extinction, being sensitive only to dust, no analogous set of lines exists in the UV (1220–3200Å). As a result, disentangling dust effects from intrinsic spectral variations is challenging in that regime.

Despite the complexity of dust geometry in galaxies, Calzetti et al. (1994) demonstrated that it is possible to empirically derive the shape of the dust attenuation curve by using two measurable quantities: the Balmer optical depth τ_B^l, which traces dust affecting nebular lines, and the UV slope β, which characterizes the reddening of the stellar continuum. The key assumption is that β and τ_B^l are linearly correlated, which implies that, on average, dust behaves like a uniform screen in front of the emitting sources (as discussed in Section

1.1.2). While this "foreground screen" model is a simplification—especially in the context of extended and clumpy star-forming regions—Calzetti et al. (1994) noted that even a clumpy dust distribution can mimic a screen-like behavior if the number of clumps along the line of sight is large ($\mathcal{N} > 10$). In that regime, the attenuation becomes effectively linear with dust content, and deviations from linearity are smaller than the intrinsic scatter of the data.
Therefore, the observed linear relation between β and τ_B^l provides empirical justification for modeling dust attenuation as a screen, at least statistically. This greatly simplifies the derivation of the attenuation law, since no a priori assumption is made about its shape. Instead, τ_B^l can be used as an independent variable, allowing the attenuation curve to be constructed empirically. A further advantage of this approach is its applicability to integrated galaxy spectra. Although galaxies host complex mixtures of stellar populations of different ages—making it impossible to know the intrinsic (unreddened) spectrum for each galaxy—one can average out population differences by binning galaxies by τ_B^l. In doing so, the variations in UV slope within a bin are dominated by dust effects rather than stellar aging. As explained in Section 1.2.3, the SEDs of galaxies in different τ_B^l bins can be compared. Their ratios reveal the shape of the attenuation curve. This statistical method avoids requiring knowledge of individual stellar populations and instead exploits the large sample size to isolate the imprint of dust attenuation.
The present work builds upon the approach developed by Calzetti et al. (1994), extending it to the context of high-redshift galaxies.

1.2.1 Balmer Optical Depth

The dust attenuation in a galaxy can be measured from the optical depth, $\tau(\lambda)$. For the simple case of a uniform layer of dust between a source of intensity I_λ^0, and the observer, the optical depth is defined as:

$$I_\lambda = I_\lambda^0 \cdot e^{-\tau(\lambda)} \tag{1.19}$$

where I_λ is the observed intensity and all quantities are dependent on the wavelength. If the optical depth is positive, it means that the emission is significantly reduced by dust.
In the case of a point source such as a star with a well-characterized SED, the optical depth can easily be determined by comparing the observed and intrinsic SEDs. However, in the case of entire galaxies for which the underlying SED is strongly affected by many factors, including the underlying stellar population, star formation history, and IMF, this becomes much more difficult.
According to Calzetti (2001), a way to estimate the dust attenuation of a galaxy, that is relatively insensitive to the underlying stellar population and IMF, is given by the flux ratio of Hα and Hβ emission lines.
These lines are Balmer emission lines, arising from the recombination and subsequent cascade of electrons to the n = 2 level of hydrogen. While collisional excitation can also contribute to the Balmer line emission in hot media (see e.g. Ferland et al. (2009)), photoionization and recombination are the predominant energetic processes in most galaxies.
The Hα line corresponds to the transition from n = 3 to n = 2, with the emission of a photon at a wavelength of $\lambda_{\mathrm{H}\alpha} = 6563$Å; while the H$\beta$ line corresponds to the transition n = 4 $\rightarrow$ 2, with $\lambda_{\mathrm{H}\beta} = 4861$Å.
Since dust absorbs mainly the bluer wavelength, the Balmer line ratio Hα/Hβ allows us to characterize the dust extinction in the regions where the nebular lines are produced, like HII regions near young and massive stars. Indeed, the intrinsic flux ratio is well determined,

since is set by quantum mechanics and is only affected by the electron temperature, T_e, and density, n_e, at the $\sim 5-10\%$ level (**?**). So it has a weak dependence on the parameters of the ionized gas. In this way, the difference between the measured ratios of the Balmer lines and the intrinsic values can be used to determine the reddening of galaxies, according to (1.20):

$$\tau_B^l = \tau_{H\beta} - \tau_{H\alpha} = \ln\left(\frac{F(H\alpha)/F(H\beta)}{2.75}\right) \tag{1.20}$$

where the superscript l indicates that τ_B has been obtained from emission line and should be distinguished from optical depths associated with the stellar continuum; while the value 2.75 comes from the theoretical value expected from the unreddened ratio $H\alpha/H\beta$ undergoing Case B recombination with $T_e = 2 \cdot 10^4 K$ and $n_e = 10^2 cm^{-3}$. Since we are considering galaxies at $z > 1.8$ we chose the intrinsic value of ratio corresponding to the temperature $T_e = 2 \cdot 10^4 K$, instead of $T_e = 10^4 K$ of the works of Calzetti et al. (1994), Battisti et al. (2016), Reddy et al. (2015) which corresponds to the unreddened ratio of 2.86.
A key point in Calzetti et al. (1994) is that the Balmer optical depth does not depend on any assumption on the extinction law.

1.2.2 UV Spectral Slope

In the UV spectral region, no set of lines comparable to the Balmer lines exists for galaxies, and the dust manifest itself in the depression of the intrinsic continuum. Consequently, the shape of the observed UV continuum can, in principle, be used to infer dust attenuation.

In actively star-forming galaxies, where the UV emission is dominated by recent star formation, and thus by young and massive stars, dust attenuation can be quantified using the UV spectral slope, β, defined by:

$$F(\lambda) \propto \lambda^{\beta} \tag{1.21}$$

where $F(\lambda)$ is the flux density between 1250 Å and 2600 Å. The presence of younger stars results in a steeper, more negative β. As dust absorbs UV photons and re-emits energy in the infrared, β becomes less negative —i.e., redder—due to attenuation (Salim and Narayanan (2020)).
However, it's important to note that β corresponds to the observed UV continuum slope and does not account for the intrinsic properties of the underlying stellar population. As a result, a galaxy with an older stellar population—where the UV flux is dominated by A-type or later stars—can exhibit the same β value as a younger, dust-reddened galaxy whose UV emission is primarily from OB stars. This degeneracy complicates the interpretation of β as a pure tracer of dust attenuation.
The contamination from older populations is especially relevant in systems with low specific star formation rates (sSFRs), where the current production of UV-bright massive stars is low. As noted by Reddy et al. (2015), this effect increases the scatter in β at fixed optical depth, and may even steepen the β–τ relation if dustier galaxies are also, on average, older and more massive.
Therefore, while a correlation between β and τ_B^l is expected if β traces dust, some intrinsic scatter is inevitable. This dispersion cannot be attributed solely to measurement

uncertainties; it also reflects variations in SFH, stellar metallicity, dust geometry, and grain composition.

The UV power-law index β can be measured from observed FUV and NUV photometry according to Battisti et al. (2016):

$$\beta = \frac{\log[F_\lambda(\mathrm{FUV})/F_\lambda(\mathrm{NUV})]}{\log[\lambda_{\mathrm{FUV}}/\lambda_{\mathrm{NUV}}]} \tag{1.22}$$

where the flux density F_λ is in $erg\ s^{-1}cm^{-2}\text{Å}^{-1}$. Typical values of the UV continuum slope β range from ~ -2.5 in young, dust-free star-forming galaxies to ~ 0 or higher in heavily dust-obscured or evolved systems (e.g., Calzetti et al. (1994); Reddy et al. (2015); Salim and Narayanan (2020)).

1.2.3 Dust Attenuation Curve

Following Calzetti et al. (1994) and Battisti et al. (2016), in order to characterize the dust attenuation curve of galaxies, we define a rescaled optical depth. Given n templates of average SEDs binned in τ_B^l, and a reference spectrum $F_r(\lambda)$, selected among the n templates (with $r < n$), the rescaled optical depth is defined as:

$$Q_{n,r}(\lambda) = \frac{\tau_{n,r}(\lambda)}{\delta\tau^l_{Bn,r}} \tag{1.23}$$

where:

$$\tau_{n,r}(\lambda) = -\ln\frac{F_n(\lambda)}{F_r(\lambda)} \tag{1.24}$$

corresponds to the dust optical depth of template n with flux density $F_n(\lambda)$, and:

$$\delta\tau^l_{Bn,r} = \tau^l_{Bn} - \tau^l_{Br} \tag{1.25}$$

is the difference between the Balmer optical depth of template n and r.

Since the templates are spectral averages of different galaxies, i.e. at different distances and with different luminosities, the equation (1.23) give us informations on the *selective* attenuation, but not on the *total* attenuation, implying that the zero-point of $Q_{n,r}(\lambda)$ is arbitrary. We set $Q_{n,r}(5500\text{Å}) = 0$ as the zero-point. Since each function is weighted by its associated $\tau^l_{Bn,r}$, we compute the average of the templates $Q_{n,r}(\lambda)$ to derive an effective selection curve, $Q_{\mathit{eff}}(\lambda)$. The effective selection curve can be related to the total attenuation curve:

$$k(\lambda) = fQ(\lambda) + R_V \tag{1.26}$$

where the factor f acts to change the tilt of the curve to make $\mathrm{k(B)} - \mathrm{k(V)} \equiv 1$, where B and V bands corresponds to $\lambda = 4400\text{Å}$ and $\lambda = 5500\text{Å}$, respectively. Physically, the term f accounts for the difference in reddening affecting the ionized gas compared to the stellar continuum. This factor can be quantitatively described by expressing the differential reddening between the two components through a reformulation of each term on the right-hand side of equation 1.23. Assuming that the reference source has $\tau^l_B = 0$, and using the definition of total extinction 1.16, the numerator can be written as:

$$\tau_n(\lambda) = -\ln\frac{F_n(\lambda)}{F_0(\lambda)} = 0.921\mathrm{A}_\lambda = 0.921\mathrm{E(B-V)}_{\mathrm{star}}\mathrm{k}(\lambda) \tag{1.27}$$

while the denominator is:

$$\delta\tau_B^l = \tau_B^l - \tau_{B0}^l = \frac{\mathrm{k(H}\beta) - \mathrm{k(H}\alpha)}{1.086}\mathrm{E(B-V)}_{\mathrm{gas}} \tag{1.28}$$

where k(Hβ) and k(Hα) are the values for the intrinsic extinction curve of the galaxy and not from the attenuation curve. Therefore, equation 1.23 can be rewritten as:

$$Q(\lambda) = \frac{\mathrm{k}(\lambda) - \mathrm{R_V}}{\mathrm{k(H}\beta) - \mathrm{k(H}\alpha)}\frac{\mathrm{E(B-V)}_{\mathrm{star}}}{\mathrm{E(B-V)}_{\mathrm{gas}}} \tag{1.29}$$

where the term $\mathrm{R_V}$ is explicity added to account for the zero-point normalization that was applied at 5500Å. By comparison of this equation, to 1.23, we find that the term f is equivalent to:

$$f = \frac{\mathrm{k(H}\beta) - \mathrm{k(H}\alpha)}{\mathrm{E(B-V)}_{\mathrm{star}}/\mathrm{E(B-V)}_{\mathrm{gas}}} \tag{1.30}$$

For extinction curves like that of the Milky Way, $E(B-V)_{\mathrm{star}} = E(B-V)_{\mathrm{gas}}$, and f corresponds simply to the difference in extinction between the Balmer emission lines. However, this equivalence does not hold for attenuation curves, where it is typically observed that $E(B-V)_{\mathrm{star}} < E(B-V)_{\mathrm{gas}}$.
Therefore, $fQ(\lambda)$ is the actual selective attenuation curve, representing the true wavelength-dependent behavior of the attenuation curve on the stellar continuum. Nonetheless, it does not correspond to a total attenuation curve unless the normalization factor, $\mathrm{R_V}$ is known. We reiterate that, since $Q_{eff}(\lambda)$ is computed using galaxies with different luminosities and at different redshifts, the normalization of the attenuation curve must be determined separately. Nonetheless, $Q_{eff}(\lambda)$ is useful in two respects: it indicates the wavelength dependence of the obscuration of the stellar continuum and the optical depth to dust of the continuum relative to the Balmer lines (Reddy et al. (2015)).

1.3 High-z Recent Results

Battisti et al. (2016) followed the methodology introduced by Calzetti et al. (1994), which was originally applied to a sample of $\sim$ 39 local starburst galaxies. By combining optical spectra from SDSS (Abazajian et al. (2009)) and ultraviolet photometry from GALEX (Martin et al. (2005)), they analyzed dust attenuation in over 900 local star-forming galaxies ($z \lesssim 0.1$) and derived a statistically robust average attenuation curve. This study confirmed several key findings of Calzetti et al. (1994): the derived curve is qualitatively consistent with the Calzetti law; the stellar continuum attenuation is systematically lower than that measured from nebular emission lines; and the observed scatter in UV slope β at low τ_B^l suggests that variations in dust geometry are not the primary driver of the dispersion.
Beyond these important studies on the dust attenuation curves of local galaxies, several works have extended the same methodology to galaxies at higher redshifts.

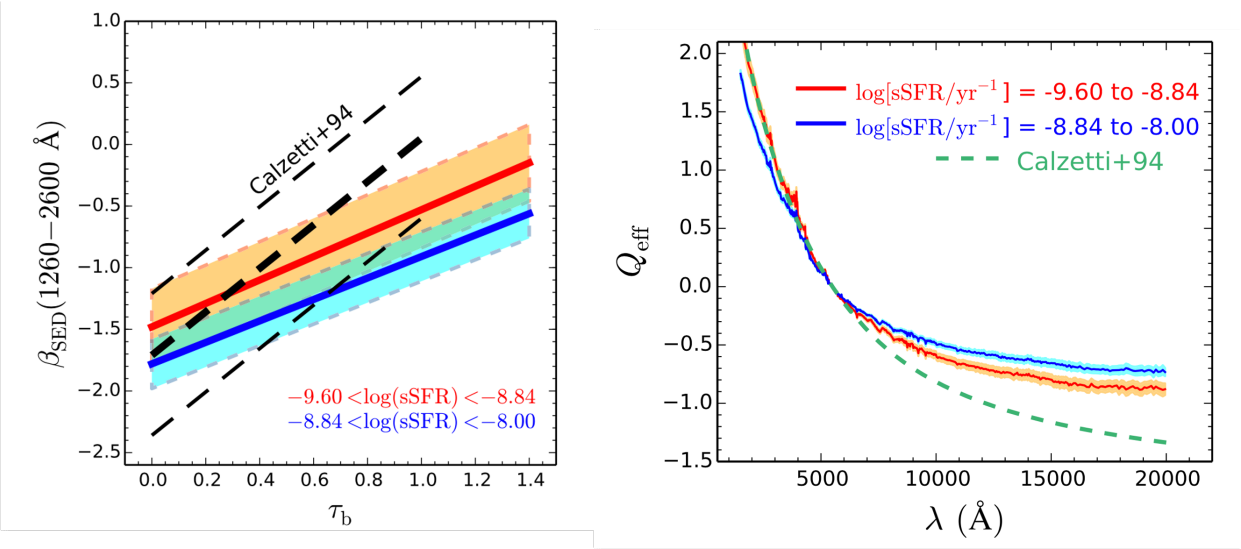

Figure 1.7: Left panel: Linear regressions between β_{SED} and τ_b. The solid lines and shaded regions indicate the best-fit linear functions and estimated intrinsic scatter for the different bins of sSFR; Right panel: effective attenuation curves (Q_{eff}) for each sSFR bin, Reddy et al. (2015).

Reddy et al. (2015) explored a sample of $\sim$ 224 star-forming galaxies at $z = 1.36 - 2.59$. To this end, they used Hα and Hβ emission line measurements from the MOSDEF survey (Kriek et al. (2015)), and constructed average SEDs combining HST photometric data. They grouped galaxies in bins of sSFR and identified a "sequence" in the distribution of galaxies within the β–τ_B^l plane as a function of sSFR, where the locus shifts toward redder β values at fixed τ_B^l with decreasing sSFR. They found the Q_{eff} in the two sSFR bin have different trends in the UV: an higher sSFR correspond to a grayer attenuation in the UV, even if the two curves are quite similar. Both curves appear to deviate at long wavelengths relative to the Calzetti et al. (1994) attenuation curve (Figure 1.7). In the end they found that the degree to which $E(B-V)_{gas}$ diverges from $E(B-V)_{stars}$ depends on sSFR of the galaxy, with the largest difference for galaxies with the largest sSFRs (Figure 1.8).

Shivaei et al. (2020) derived the UV–optical stellar dust attenuation curve for galaxies at redshift z = 1.4–2.6 as a function of gas-phase metallicity. Their analysis is based on a sample of $\sim$218 star-forming galaxies from the MOSDEF survey (Kriek et al. (2015)), with robust spectroscopic measurements of Hα, Hβ, and [NII] emission lines obtained using Keck-/MOSFIRE spectrograph (Mclean et al. (2010)). They computed the effective attenuation curve ($k_\lambda - R_V$) in two metallicity bins, separated at $12 + \log(O/H) = 8.5$.
The low-metallicity curve appears to show a steep UV rise similar to that of the SMC curve. In contrast, the high-metallicity curve has a slope consistent with the Calzetti et al. (1994) curve and is best fitted with a UV bump at 2175Å as shown in Figure 1.9. This result may be attributed either to differences in dust grain properties between low- and high-metallicity environments, or to variations in the spatial distribution of dust and stars. In the latter case, the steeper attenuation curve seen in low-metallicity galaxies could arise from a greater fraction of young stars still embedded in their natal clouds, experiencing stronger attenuation at shorter wavelengths. The former scenario proposes that small dust grains—responsible for the UV rise—are more prevalent in low-metallicity environments, either as a result of the fragmentation of larger grains under intense ionizing radiation and/or because of the low fraction of molecular clouds for dust grains to hide in.
They also find that the ionized gas reddening is, on average, $\sim$ 2 times larger than the

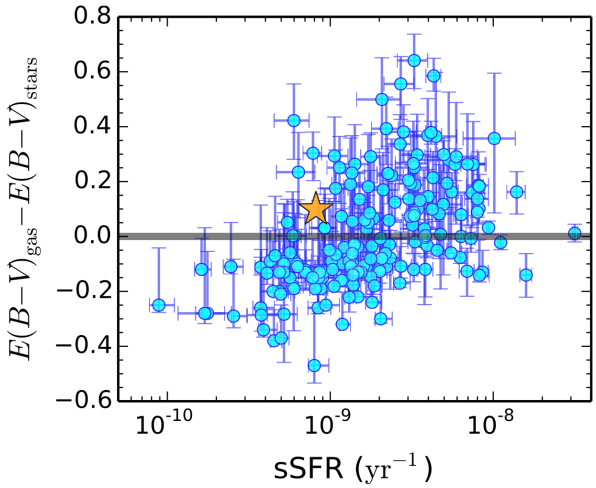

Figure 1.8: Difference between the gas and continuum color excesses as a function of sSFR, where the solid line indicates no difference between the color excess of the nebular regions and the stellar continuum. The large star denotes the average values for the Hβ-undetected galaxies, Reddy et al. (2015).

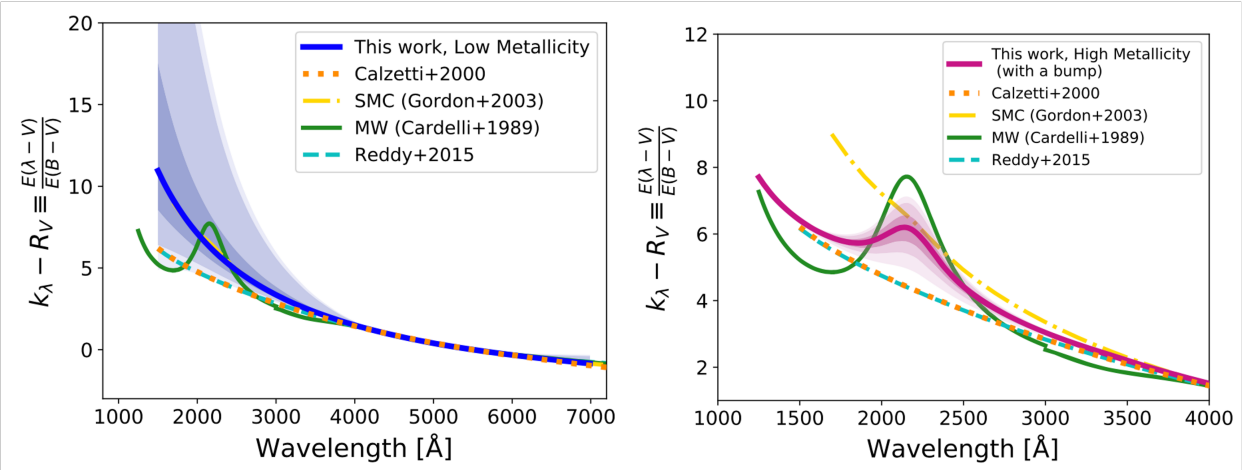

Figure 1.9: Stellar attenuation curves at z=1.4–2.6 for the two samples with gas-phase metallicities below and above 12 + log(O/H) = 8.5, Shivaei et al. (2020).

stellar continuum reddening at low metallicities, and is similar to the continuum reddening at high metallicities (Figure 1.10).

Battisti et al. (2022) explored the effect of dust on $\sim$ 900 galaxies at $z \sim 1.3$ with HST grism surveys (Atek et al. (2010); Brammer et al. (2012)). They found the $\beta - \tau_B^l$ relation and the average dust attenuation curve using stacked spectra, binned by (Hα+[NII])/[OIII] line ratio. They found values for the slope S and normalization R_V intermediate between the findings of Calzetti et al. (1994) at $z \sim 0$, and Reddy et al. (2015) at $z \sim 2$ (Figure 1.11), suggesting a redshift evolution. The intensity of the UV bump shows values similar to those found in other SED-based studies at various redshifts, suggesting that the bump may depend more strongly on metallicity (Shivaei et al. (2020)) than on redshift.

This thesis presents the first study to explore the empirical dust attenuation curve over the wide redshift range of $2 \lesssim z \lesssim 7$ using JADES spectroscopy (D'Eugenio et al. (2024)), following the methodology proposed by Calzetti et al. (1994). In Chapter 2, we present the

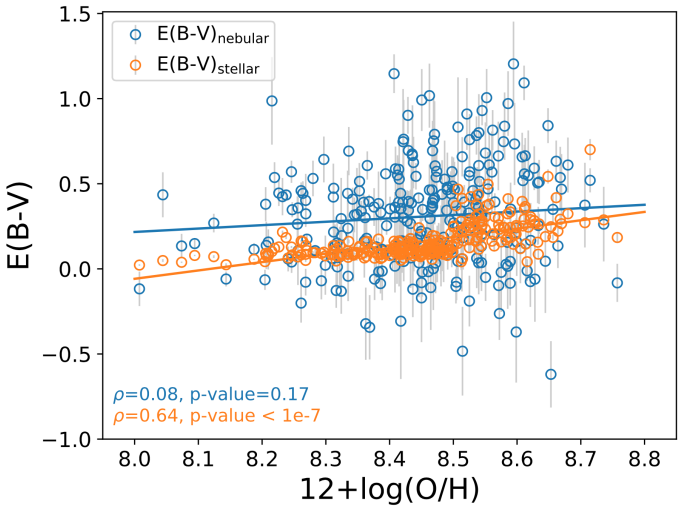

Figure 1.10: Nebular (blue) and stellar (orange) reddening as a function of metallicity. The linear regression fits are shown with solid lines. Both nebular and stellar reddening increase with increasing metallicity, although the trend is weak for nebular reddening vs. metallicity, Shivaei et al. (2020).

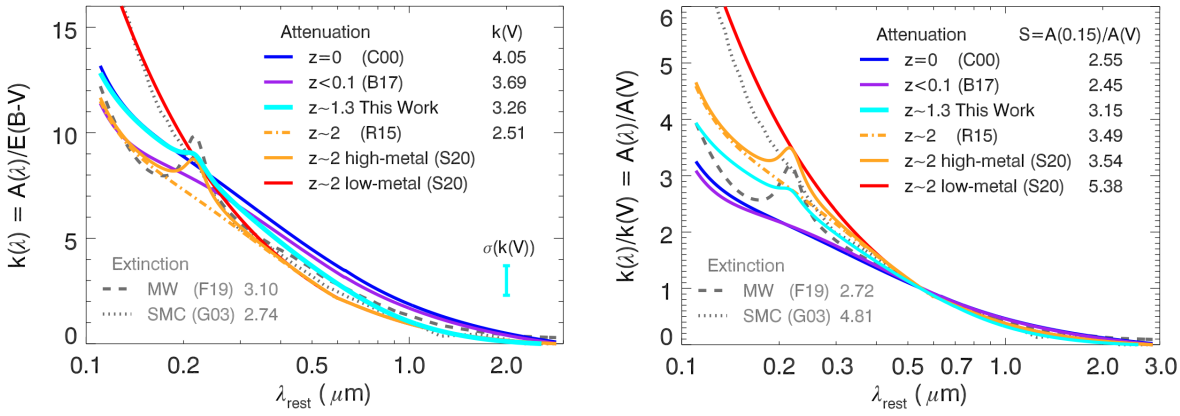

Figure 1.11: Left-hand panel: Total-to-selective dust attenuation curve, $k(\lambda)$, for $z \sim 1.3$ sample (cyan line) compared to other studies using the same Balmer decrement technique at other redshifts (colour lines), with the curve normalization, k(V), for each also denoted. The extinction curves for the MW and SMC are also shown for reference (gray lines). Right-hand panel: Similar to left, but showing the normalized dust attenuation curve, k(λ)/k(V), with the UV curve slope, S = A(0.15)/A(V), for each also denoted. The values of k(V) and S at $z \sim 1.3$ lie in-between those at $z \sim 0$ and $z \sim 2$, supporting the notion that the average values of these quantities evolve with redshift, Battisti et al. (2022).

photometric and spectroscopic datasets and detail the sample selection criteria. Chapter 3 outlines the SED fitting procedures used to derive galaxy physical properties and describes the implementation of the methodology introduced by Calzetti et al. (1994). In Chapter 4, we report our main findings, including sample characteristics, average spectral energy distributions (SEDs), and the derived attenuation curves. Finally, Chapter 5 is devoted to the discussion and interpretation of the results.

Chapter 2

A JWST Spectroscopic Sample at $2 < z < 7$

2.1 JADES and ASTRODEEP Catalogs

The dataset used includes both spectroscopic and photometric data from the GOODS-North and GOODS-South fields. In fact, the aim of this study is to characterize the dust attenuation curve at high redshifts and explore its connection to the physical properties of galaxies.

The spectroscopic sample is represented by the third data release of JADES, the JWST Advanced Deep Extragalactic Survey (D'Eugenio et al. (2024)). It provides both imaging and spectroscopy into the two GOODS fields.
The photometric catalog is provided by the ASTRODEEP-JWST project (Merlin et al. (2024)) aimed at studying early galaxy formation and evolution in the high-redshift Universe. It provides NIRCam-HST multiband photometry and redshifts for half a million sources in six extragalactic deep fields.

Spectroscopy consists of medium-depth and deep NIRSpec/MSA spectra of 4,000 targets, covering the spectral range 0.6–5.3 μm and observed with both the low-dispersion prism ($R = 30$–300) and all three medium-resolution gratings ($R = 500$–1500), that are G140M, G235M, and G395M.
The data release includes 1-d and 2-d fully reduced spectra, with slit-loss corrections and background subtraction optimized for point sources. For extended sources, which are also of interest in our study, slit-loss correction is not provided. Moreover, the spectra are not corrected for Galactic extinction. Therefore, we applied corrections for both slit losses and Galactic extinction, as described in Section 3.3.
Spectroscopic redshifts and $S/N > 5$ emission-line flux catalogs for the prism and grating spectra are provided, and the targets span from redshift $z = 0.5$ up to $z = 13$.
To date, this dataset constitutes the most extensive statistical foundation for investigating the physical characteristics of galaxy populations formed during the Universe's first billion years.

The ASTRODEEP catalog gathers data from eight JWST NIRCam observational programs, targeting the Abell 2744 (GLASS-JWST, UNCOVER, DDT2756 and GO3990), EGS (CEERS), COSMOS and UDS (PRIMER), and GOODS North and South (JADES and NGDEEP) deep fields, for a total area of $\simeq 0.2$ sq. degrees. Data from the JADES

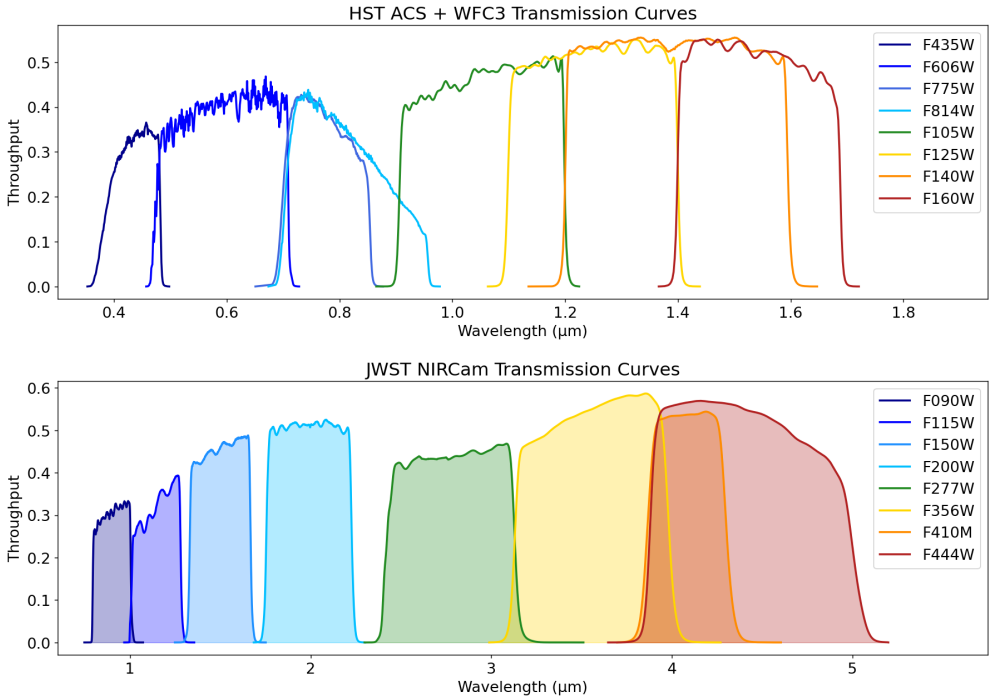

Figure 2.1: Transmission curves of the HST ACS and WFC3 filters (top panel) and JWST NIRCam filters (bottom panel), showing mean system throughputs.

program, of our interest, cover an area of $\simeq$ 83.0 sq. arcmin in the GOODS-North region (JADES-GN hereafter), and of $\simeq$ 84.5 sq. arcmin in the GOODS-South region (JADES-GS hereafter).
Moreover, new measurements from HST archival data are included, thus collecting 16 bands spanning from 0.44 to 4.44 μm.
The chosen bands are: HST ACS F435W, F606W, F775W and F814W; HST WFC3 F105W, F125W, F140W and F160W; and NIRCam F090W, F115W, F150W, F200W, F277W, F356W, F410M and F444W. The mean system throughputs of such filters are are taken from the SVO Filter Profile Service[1] and plotted in Figure 2.1.

All the total fluxes were corrected for the effect of galactic extinction through the use of the NASA/IPAC Extragalactic Database (NED)[2] extinction calculator.

2.2 Sample Selection

The JADES Data Release 3 provides spectra for 4086 targets located in the GOODS-North and GOODS-South fields. The subsequent sample selection is based on two key requirements: availability of Hα and Hβ emission line fluxes for estimating the Balmer optical depth, τ_B^l, and photometric fluxes in the UV rest-frame to derive the UV-β slope.

We first selected the targets with available Hα and Hβ emission line fluxes, using the fast selection tools provided by the `TOPCAT`[3] software.

In this way, we obtained 627 targets from the low-dispersion prism spectra and 585 targets from the medium-resolution gratings. We then excluded data flagged by the *DR-flags*

[1]SVO Filter Profile Service: svo2.cab.intacsic.es
[2]Extinction calculator: ned.ipac.caltech.edu/extinction_calculator
[3]An interactive graphical viewer and editor for tabular data.

indicator, which identifies spectra affected by data reduction issues or shutter problems (including cases with low-level contamination). After this filtering, we ended up with two separate samples: 545 targets from the low-dispersion prism spectra and 584 targets from the medium-resolution gratings.

Furthermore, the low-dispersion prism does not have sufficient resolution to fully resolve the Hα emission line. It only provides a single component which is a blend of Hα and [NII]6584, but we need precise measurements of emission lines to study the Balmer decrement. For this reason we decided to use the medium-resolution gratings data, in which Hα and Hβ emission lines are fully resolved thanks to its better resolution.

We then performed a cross-match between the spectroscopic and photometric catalogs, selecting matches based on coordinate agreement within 1 *arcsec*
The resulting sample comprises 534 galaxies, with redshifts ranging from $z \sim 0.6$ to $z \sim 6.9$.

2.2.1 Parameter Constraints and Sample Cleaning

Starting with the selected sample of 534 sources, several cuts were applied during the parameter estimation procedure — specifically, for the computation of τ_B^l and β — as well as in the spectral analysis, to ensure the quality of the spectra.

As a first step, we cross-matched our catalog with the slit-loss correction parameter catalog for JADES targets, provided by Pietro Benotto and described in Section 3.3. Since 30 sources lacked slit loss correction values, we excluded them from our sample.

Then, as previously mentioned, flux measurements in the near-UV (NUV) and far-UV (FUV) rest-frame bands—centered at $\lambda_{\mathrm{NUV}} = 2267$ Å and $\lambda_{\mathrm{FUV}} = 1516$ Å, respectively—are required to compute the UV-β slope as defined in equation (1.22). However, our photometric filters cover a wavelength range starting from $\lambda_{ref} = 4329$ Å so we lack measurements for the FUV rest-frame flux at lower redshifts. Therefore, only objects with rest-frame photometry covering the UV slope were considered. According to the redshift definition (2.1):

$$\lambda_{obs} = \lambda \cdot (1 + z) \tag{2.1}$$

where the emitted wavelengths λ correspond to the NUV and FUV rest-frame wavelengths, our analysis includes targets with redshifts $z > 1.84$, excluding 74 targets.
Moreover, 5 targets have been discarded during the computation of β, due to the quality of photometric data in the bands of interest. More details about this selection procedure are provided in Section 3.2. We also excluded two targets for which the uncertainties exceeded the measured flux values (e.g., $\sigma_{\mathrm{FUV}} > F_{\mathrm{FUV}}$).

Subsequently, we focused on the computation of τ_B^l. As a first step, we discarded sources with unreliable Hα and Hβ fluxes — specifically, those with negative values or with $F_{\mathrm{H}\alpha} < F_{\mathrm{H}\beta}$. This led to the removal of 4 targets.

At this point, we checked if there were some AGN in the sample. In fact, in the context of AGN, the interpretation of the Balmer decrement is more complex due to the extreme physical conditions present in the emission regions.
21 AGN have been found in our sample, provided by the works of Maiolino et al. (2024) and Scholtz, Jan et al. (2025). Section 2.2.2 provides further insight into this topic.

After these selection steps, 64 sources exhibited negative values of τ_B^l, which are non-physical, as they violate basic principles of quantum mechanics: $\tau_B^l < 0$, means that the

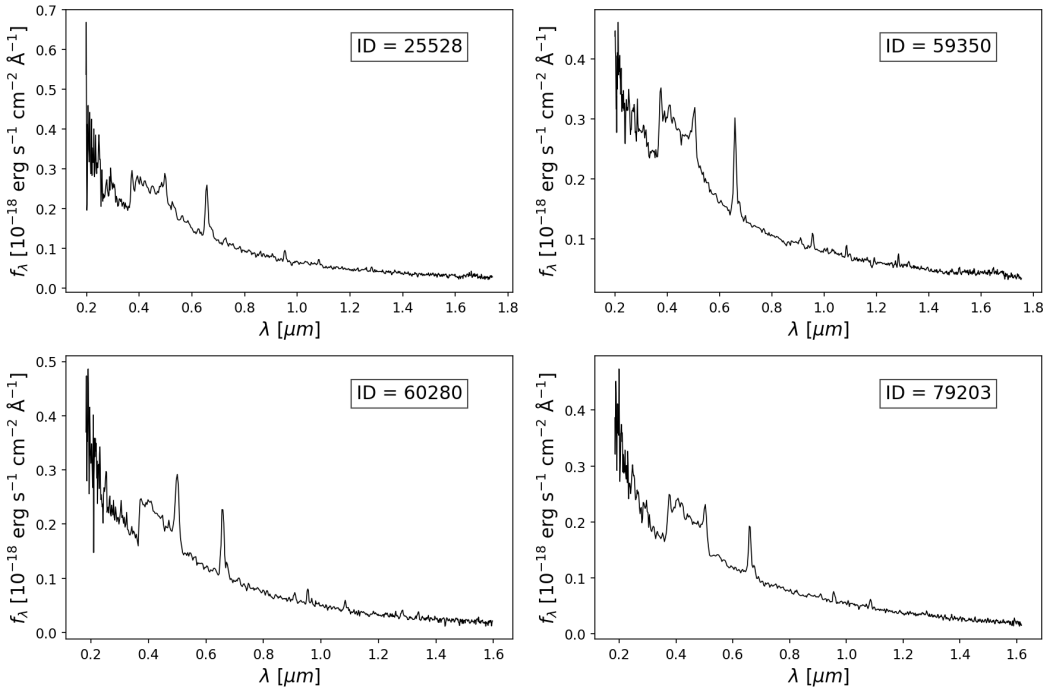

Figure 2.2: Example sources displaying the shutter bump in the rest-frame continuum.

observed ratio Hα/Hβ is smaller than the intrinsic one, in absence of dust. This could be related to uncertainties in the measure of the emission fluxes, or from variations in the environment in which we should evaluate the intrinsic ratio: for $T_e > 2 \cdot 10^4$K end/or $n_e > 10^2 cm^{-3}$ the intrinsic ratio decreases (Battisti et al. (2016)). Therefore, these targets were excluded from the sample.

As a final step of the selection, the spectral quality was verified.
By visual inspection, we identified a spurious bump in the rest-frame continuum around 0.4 μm in some sources. This feature was attributed to a shutter-related artifact, and the affected targets were consequently excluded from the final sample. A total of 12 sources were identified as affected by the so-called "shutter bump" feature, with examples shown in Figure 2.2.

After that, we visually inspected the spectra to evaluate the prominence of the Balmer break—a discontinuity at 4000 Å that is linked to the average age of the stellar population. This feature is quantified by the $D_n(4000)$ index: low values of $D_n(4000)$ are associated with young galaxies dominated by hot, massive (blue) stars, whereas high values indicate older stellar populations dominated by cooler, red stars. Including targets with a wide range of $D_n(4000)$ values in the sample can bias the derivation of the attenuation curve. In particular, galaxies with intrinsically redder continua due to older stellar populations may artificially inflate the estimated attenuation in the blue region ($\lambda < 5500$ Å), leading to an overestimation of dust effects. Because reliably measuring $D_n(4000)$ at high redshift is non-trivial, we opted to exclude from the sample those targets exhibiting a very prominent Balmer break compared to the majority of the sample, as these likely correspond to evolved, older stellar populations. We selected 3 targets with this feature, showed in Figure 2.3.

In the end, we examined the continuum SNR. As explained in Chapter 4, the construction of the selective attenuation curve relies on the creation of average SEDs in τ_B^l bins. Since the most informative part of the attenuation curve lies in the UV region — which is also the

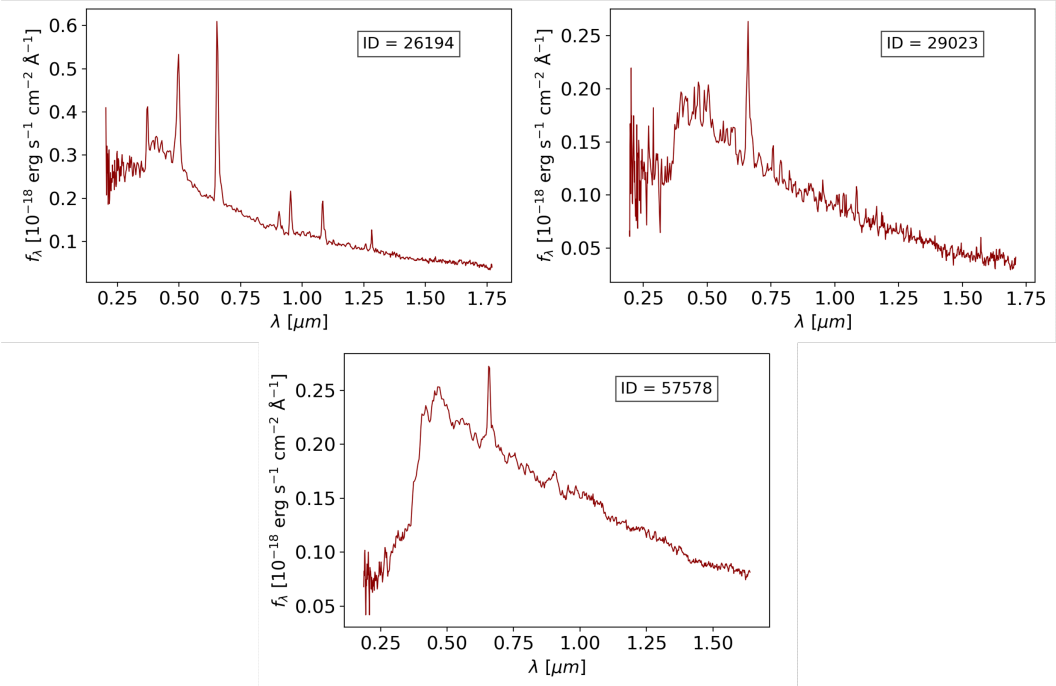

Figure 2.3: Example sources displaying an high Balmer break in the rest-frame continuum.

noisiest due to the limited resolving power of the prism — we retained only sources with SNR > 2 in the rest-frame interval $0.15\ \mu\text{m} < \lambda < 0.40\ \mu\text{m}$, in order to better constrain the shape of the selective attenuation curve. This step led to the removal of 18 targets from the sample.
This constraint may introduce potential biases, as faint, high-redshift, or heavily dust-obscured galaxies tend to have lower UV fluxes and thus lower SNR in that region. However, the excluded targets all exhibit relatively low Balmer optical depths ($\tau_B^l \lesssim 0.5$), indicating that they are not significantly dust-obscured. Therefore, this cut does not bias the sample against dusty galaxies.
Regarding redshift bias, we find that the SNR-based cut introduces a mild redshift-dependent selection effect. The median redshift of excluded sources is $z = 4.22$, compared to $z = 3.47$ for the original sample and $z = 3.46$ for the remaining targets. This suggests that the SNR cut preferentially removes higher-redshift galaxies, likely due to decreased line detectability at higher redshifts. Although the impact is limited in our current sample, we will take this potential bias into account in future analyses, particularly when increasing the sample size. In Figure 2.4 we show the redshift distribution of the sample before and after the SNR-based cut cut.

Table 2.1 summarizes all the steps involved in the sample selection process, along with the corresponding sample sizes.

2.2.2 AGN

AGN are often considered extreme objects in astronomy due to their exceptionally high luminosities, relativistic jets, rapid variability, and the extreme physical conditions surrounding the supermassive black holes at their centers. These features make the interpretation of emission line luminosities and the Balmer decrement particularly challenging.

In AGN, two distinct emission regions are typically identified, each with different charac-

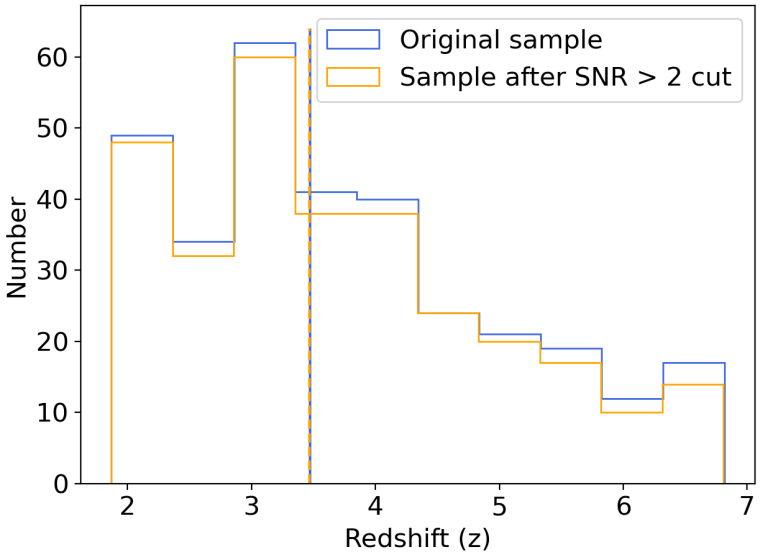

Figure 2.4: Redshift distribution of the original spectroscopic sample (blue) and of the subset selected after applying a SNR > 2 cut on the continuum in the rest-frame interval $0.15\ \mu\text{m} < \lambda < 0.40\ \mu\text{m}$ (orange). Vertical lines indicate the median redshifts of each distribution. The cut preferentially excludes higher-redshift galaxies, introducing a mild redshift-dependent selection bias. However, the effect is limited in the current sample.

teristics: the Broad Line Region (BLR) and the Narrow Line Region (NLR).
The BLR is located closer to the supermassive black hole of the AGN and is strongly influenced by its gravitational field. It contains high-density gas moving at high velocities (up to thousands of km/s), producing broad emission lines in the spectrum due to the Doppler effect. The NLR, on the other hand, is found at greater distances from the black hole compared to the BLR. It contains lower-density gas, ionized by the AGN radiation, and produces narrower emission lines, with typical velocities of a few hundred km/s.

Lu et al. (2018) found that the NLR is subject to more reddening by dust than the broad-line region (BLR), and that $\text{H}\alpha^{\text{b}}/\text{H}\beta^{\text{b}}$ does not correlate with $\text{H}\alpha^{\text{n}}/\text{H}\beta^{\text{n}}$. But more importantly they found that Balmer decrements have no correlation with optical luminosity, but show some dependence on accretion rate: in the NLR, the accretion rate could indirectly affect dust extinction or the physics of the ionized gas, whereas in the BLR, no clear dependence is observed.

Recently, Wu et al. (2023) found that variations in the Balmer decrement can also be influenced by changes in AGN activity. For instance, in some low-luminosity AGNs and "changing-look" AGNs, an elevated Balmer decrement might not be due to dust extinction but rather to a decrease in the ionizing photon flux associated with a low accretion rate.

Due to the complex physical conditions in their emission regions, the Balmer decrement does not have a straightforward correlation with dust extinction, as it does in normal star-forming galaxies. The presence of both broad-line and narrow-line regions, variations in accretion rate, and changes in ionizing photon flux further complicate its interpretation. For these reasons, we opted to remove known AGN—21 targets in total—from our analysis to ensure a more reliable assessment of dust extinction and gas properties in our sample.

Filtering Step	**Sample Size**	**Selection Criteria**
Initial sample	4086	JADES dr3 GOODS fields sources
Emission lines measurements	585	Sources with Hα and Hβ fluxes from medium resolution gratings
DR flag	584	Removed targets with Data Reduction problems
Match with Photometry	534	Sources with both spectroscopic and photometric data
Match with Slit Loss	504	Sources with spectra corrected for slit loss
Redshift cut	430	Sources with UV restframe spectra measurements, i.e. $z > 1.84$
UV-β slope computation	423	Removed targets with unestimable β
τ_B^l computation	419	Targets with reliable $H\alpha$ and $H\beta$ measurements
AGNs cut	398	Sample without AGNs
Non-physical τ_B^l cut	334	Sources with $\tau_B^l \geq 0$
Shutter bump feature	322	Removed spectra with strange bump feature due to telescope's shutter problems.
High $D_n(4000)$ cut	319	Removal of sources with prominent Balmer break
SNR cut	301	Sources with SNR > 2 in the region $0.15\ \mu m < \lambda < 0.40\ \mu m$

Table 2.1: Summary of the sample selection steps.

Chapter 3

Methods

In this Chapter, we describe the methods used to estimate galaxy properties—focusing in particular on the `BAGPIPES` tool—as well as the procedures for computing key parameters such as the UV spectral slope β and the Balmer optical depth τ_B^l. We also detail the construction of average SEDs used to derive the empirical dust attenuation curve.
In addition, we outline the steps taken to correct spectroscopic fluxes for the effects of Galactic extinction and slit losses (Section 3.3).

Specifically, galaxy properties were derived from photometry (Section 3.1), and the UV slope β was computed as described in Section 3.2. Medium-resolution grating spectra were used to measure the $H\alpha$ and $H\beta$ emission lines for the calculation of τ_B^l (Section 3.4), while low-dispersion prism spectra were employed to analyze the UV–optical continuum and construct average SEDs in bins of τ_B^l, for the derivation of the selective attenuation curve (Section 3.5).

3.1 SED fitting: `BAGPIPES`

Bayesian Analysis of Galaxies for Physical Inference and Parameter EStimation (`BAGPIPES`[1]) is a `Python` code used for modelling galaxy spectra and fitting these models to arbitrary combinations of spectroscopic and photometric observational data.
An important feature of `BAGPIPES` (Carnall et al. (2018)) is that it allows to model realistic emission of galaxies from the far-ultraviolet to the microwave regime.

The internal model of a galaxy spectrum can be constructed with the desired level of complexity by specifying various model features —such as global parameters, star-formation history, nebular emission and dust attenuation components— each provided as input to the API[2] as `Python` dictionaries containing parameters values.
As part of the model configuration, the user can specify the wavelength coverage of the continuum spectral data, the set of photometric filters to be used (as done in our analysis), and whether to include emission-line fluxes.

This code performes parameters estimation by utilizing a Multimodal nested sampling algorithm, `MultiNest` (Feroz and Hobson (2008), Feroz et al. (2009)).

[1] The official documentation is available at: bagpipes.readthedocs.io
[2] Application Programming Interface.

3.1.1 Model Generation

As we said previously, all of the physical parameters that the user provides when creating a *galaxy model* object are passed within the *model components* dictionary.
A model for a galaxy spectrum, observed at redshift z_{obs} is represented by the luminosity per unit rest-frame wavelength $L_\lambda(\lambda)$. This luminosity is constructed in `BAGPIPES` from a combination of four elements, according to the relationship 3.2:

(i) *Simple Stellar-Population* model, SSP(a, λ, Z), which are a function of λ, age of stellar population a, stellar metallicity Z and the initial mass function. `BAGPIPES` does not directly implement the *Stellar Population Synthesis* SPS but instead utilizes predefined models. Currently, the supported models are Bruzual and Charlot (2003), based on the MILES library for the UV-optical region. The spectra of SSP are sampled on a logarithmic age grid with a resolution of 0.1 *dex*, covering a range from 10^6 to $10^{10.2}$ years.

(ii) The *star formation history*, SFR(t), which is composed of a sum of one or more components j, that specify the functional form for star-formation rate as a function of time:

$$\mathrm{SFR(t)} = \sum_{\mathrm{j=1}}^{\mathrm{N_c}} \mathrm{SFR_j(t)} \tag{3.1}$$

(iii) The *transmission function of the ionized ISM*, $\mathrm{T^+(a, \lambda)}$, as defined by Charlot and Longhetti (2001), including absorption, line emission, ionized continuum emission and emission from warm dust within HII regions.

(iv) The *transmission function of the neutral ISM*, $\mathrm{T^0(a, \lambda)}$, accounting for diffuse dust attenuation and emission.

$$\mathrm{L_\lambda(\lambda)} = \sum_{\mathrm{j=1}}^{\mathrm{N_c}} \sum_{\mathrm{i=1}}^{\mathrm{N_a}} \mathrm{SFR_j(t_i) SSP(a_i, \lambda, Z_j) T^+(a_i, \lambda) T^0(a_i, \lambda) \Delta a_i} \tag{3.2}$$

where i runs across the age bins used in `BAGPIPES`, Δa_i are the widths of these bins, j runs across SFH components, $\mathrm{N_c}$ is the number of SFH components and $\mathrm{N_a}$ the number of age bins.
Then, the luminosity 3.2 is redshifted and converted into an observed frame flux density $f_{\lambda_{obs}}(\lambda_{obs})$, with $\lambda_{obs} = \lambda \cdot (1 + z_{obs})$, according to the 3.3:

$$f_{\lambda_{obs}} = \frac{\mathrm{L_\lambda(\lambda)}}{4\pi \mathrm{D_L}(z_{obs})^2 (1 + z_{obs})} \mathrm{T_{IGM}}(\lambda, z_{obs}) \tag{3.3}$$

where $\mathrm{D_L}(z_{obs})$ is the luminosity distance to redshift z_{obs} and $\mathrm{T_{IGM}}(\lambda, z_{obs})$ is the transmission function of the IGM.
The *model components* that can be given in input as dictionaries are:

- **Global parameters:** which can include the observed redshift, the maximum age of birth clouds, the velocity dispersion of stars, and some SFH informations;

- **Star-formation history components:** the functional component of individual $\mathrm{SFR}_j(t)$ can be specified. The total SFH is given by the sum of all the individual components as in 3.2. The functional components can be: delta function (for bursts), top-hat function, τ model, delayed-τ model, lognormal SFR, double-power law. One of these model components, plus the *total mass formed* M_{formed} and *metallicity* Z_i must be specified.
- **Nebular component:** this component tells BAGPIPES to include emission lines and nebular continuum emission in the model. These come from the CLOUDY photoionization code by Chatzikos et al. (2023) which models HII regions with a spherical shell geometry. The metallicity of the gas in the stellar birth clouds is assumed to be the same as the stars producing the ionizing flux. The only parameter that must be specified is the *ionization parameter* $\log U$.
- **Dust attenuation and emission component:** Three dust models are currently implemented: the Calzetti (2001) law for local star-forming galaxies, the Cardelli et al. (1989) Milky Way dust law, and a flexible model based on that of Charlot and Fall (2000). Then, the absolute attenuation in the V band, $\mathrm{A_V}$, must be specified. Other features can be introduced as reported in the official documentation.

3.1.2 Prescription and Results

SED fitting was carried out using photometric flux data. For this purpose, the filter transmission curves corresponding to the bands used in the analysis (shown in Figure 2.1) were provided as input.

Subsequently, we defined the model components. For the star formation history (SFH), we included the mandatory parameters: *mass-formed* (i.e., the total stellar mass formed) and *metallicity*. We adopted a single SFH model -the delayed-τ model- characterized by two parameters: *age* (the time since star formation began) and τ (the timescale of its decline), as described in Equation 3.4:

$$\mathrm{SFR}(t) \propto t \cdot \exp\left(-\frac{t}{\tau}\right) \tag{3.4}$$

The nebular component was included to account for both emission lines and nebular continuum emission. To do so, we specified the ionization parameter U.
Finally, we included a dust attenuation component by selecting the "Calzetti" law provided by BAGPIPES, along with the absolute attenuation in the V band, denoted as $\mathrm{A_V}$.

Moreover, we use the spectroscopic redshift provided by the JADES catalog as a direct input to the fitting code, in order to obtain a more accurate parameter estimation.

The priors adopted for all parameters are summarized in Table 3.1.

In Figure 3.1, we show examples of SED fitting results obtained with Bagpipes. The large number of photometric bands allows for a highly accurate fit.

The most important physical parameter for our study is the stellar mass—tightly linked to the amount of dust—and it is one of the main outputs provided by BAGPIPES. The reliability of our mass estimates was assessed by comparing them with the results obtained by Pietro Benotto (private communication), spectroscopic SED fitting using BAGPIPES with a non-parametric SFH. As shown in Figure 3.2, the two methods yield consistent estimates, indicating that no systematic effects are present in our measurements.

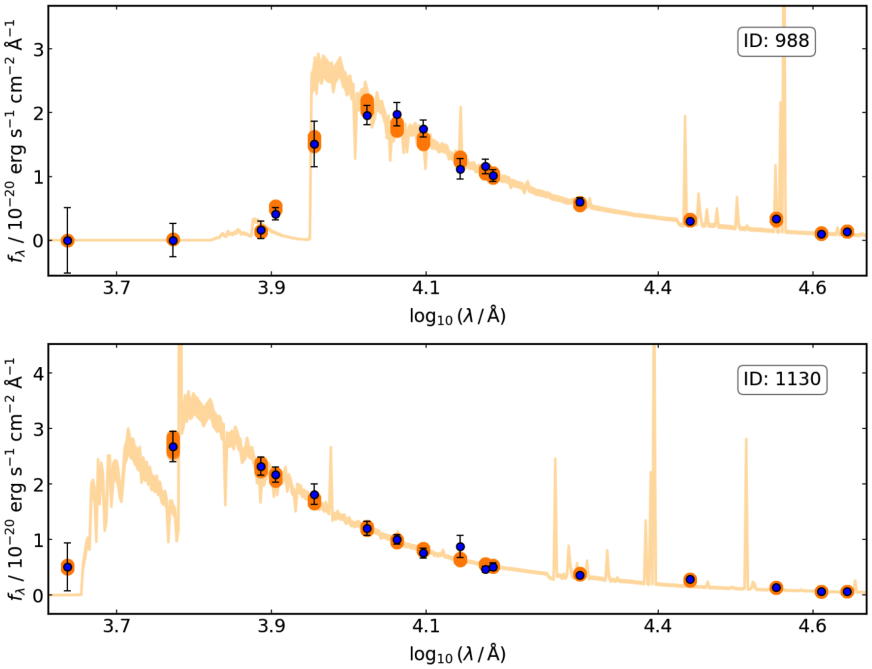

Figure 3.1: Example SED fitting results from `BAGPIPES` for targets 988 and 1130 in our sample. The orange line shows the best-fit model spectrum from `BAGPIPES`, obtained by comparing a range of synthetic spectral models with the observed photometry. Orange dots represent the model photometric fluxes derived via convolution with the spectral template, while blue dots indicate the observed fluxes with their associated uncertainties.

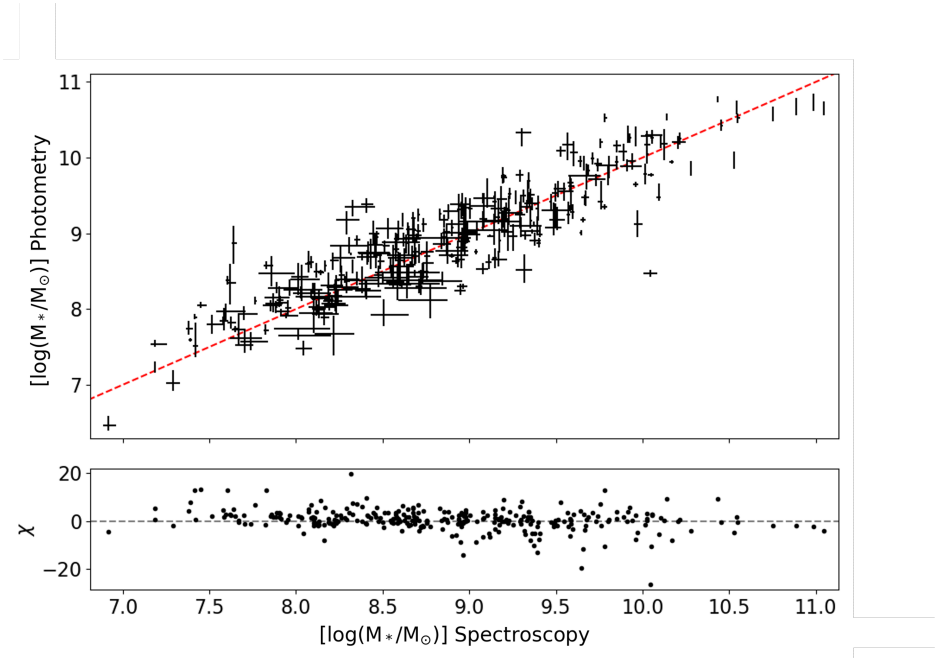

Figure 3.2: Comparison between stellar masses M_* estimated by SED fitting of our photometric data and those derived from photometric SED fitting provided by Pietro Benotto.

	parameters	prior	range
dust	A_V $[mag]$	uniform	0, 6
nebular emission	logU	uniform	-4, -1
delayed-τ model	age [Gyr]	uniform	0.001, 15
	τ [Gyr]	uniform	0.01, 10
	metallicity [$Z_\odot$]	uniform	0, 2.5
	mass-formed [$\log_{10}(M_*/M_\odot)$]	uniform	6, 12.5

Table 3.1: Priors used in the `BAGPIPES` model.

Moreover, this comparison also serves to validate the quality of the photometric data adopted in our analysis. The agreement between photometric and spectroscopic estimates further suggests that the two datasets —photometric and spectroscopic— can be effectively combined without introducing systematic effects in our study.

3.2 UV-slope Computation

For the computation of the UV spectral slope β (see Eq. 1.22), we start from the spectral flux density F_ν, provided by ASTRODEEP, and recall its conversion to F_λ:

$$F_\lambda(\lambda) = F_\nu(\nu) \cdot \frac{c}{\lambda^2} \tag{3.5}$$

However, using this relation, we can derive an equivalent expression for β directly in terms of F_ν:

$$\beta = \frac{\log\left(\frac{F_\nu(\mathrm{FUV})}{F_\nu(\mathrm{NUV})}\right) - 2\log\left(\frac{\lambda_{\mathrm{FUV}}}{\lambda_{\mathrm{NUV}}}\right)}{\log\left(\frac{\lambda_{\mathrm{FUV}}}{\lambda_{\mathrm{NUV}}}\right)} \tag{3.6}$$

where $F_\nu(\mathrm{FUV})$ and $F_\nu(\mathrm{NUV})$ are the rest-frame flux densities measured in the FUV and NUV bands, respectively.
The error associated to β is:

$$\begin{aligned}\sigma_\beta &= \sqrt{\left(\frac{\partial\beta}{\partial F_\nu(\mathrm{FUV})}\right)^2 \sigma^2_{F_\nu(\mathrm{FUV})} + \left(\frac{\partial\beta}{\partial F_\nu(\mathrm{NUV})}\right)^2 \sigma^2_{F_\nu(\mathrm{NUV})}} \\ &= \frac{\sqrt{\left(\frac{\sigma_{F_{\mathrm{FUV}}}}{F_{\mathrm{FUV}}}\right)^2 + \left(\frac{\sigma_{F_{\mathrm{NUV}}}}{F_{\mathrm{NUV}}}\right)^2}}{\ln 10 \cdot \log(\frac{\lambda_{\mathrm{FUV}}}{\lambda_{\mathrm{NUV}}})}\end{aligned} \tag{3.7}$$

To compute these values, we performed a linear interpolation—using MCMC to incorporate the associated uncertainties and estimate $\sigma_{F_{\mathrm{NUV}}}$ and $\sigma_{F_{\mathrm{FUV}}}$—between the fluxes measured in the bands covering/containing the NUV or FUV rest-frame. The fluxes were then evaluated at $\lambda_{\mathrm{NUV}} = 1516$Å and $\lambda_{\mathrm{FUV}} = 2267$Å, following the methodology described by Battisti et al. (2016).

However, some targets exhibit spurious fluxes—either flagged in the catalog (e.g., with an error code of -99.0) or showing non-physical integer values greater than 1.0. In addition, certain bands display anomalously high fluxes compared to the others, such as values exceeding 10 μJy or clearly inconsistent with the underlying continuum (e.g., likely ejecta). These cases were excluded from the analysis. Specifically, we discarded bands where the flux difference between adjacent measurements exceeded an order of magnitude, or where the uncertainty on the flux was larger than the measured flux itself.
To implement this filtering, we developed an algorithm that systematically skipped such problematic bands and continued the interpolation using the next available ones. 5 targets were removed in this step.

3.3 Spectra Correction

The previous sections have focused on the analysis of the photometric sample. Following that, we proceeded with the spectroscopic data. The photometric catalog by Merlin et al. (2024) already provides fluxes corrected for Galactic extinction. The authors made use of the NASA/IPAC Extragalactic Database (NED) extinction calculator, which returns the average extinction in each band at specified equatorial coordinates —set to the centers of the fields' FoVs.
The same procedure was applied to spectra: an interpolation between the galactic extinction coefficient (GE) in the bands provided by NED was performed. Then an extrapolation was done to extend the values to higher wavelengths, up to $5.2\mu m$. The observed fluxes F_{obs} in the band X_i was corrected using the relation 3.8:

$$F_{corr,\mathrm{GE}} = F_{obs} \cdot 10^{\frac{\mathrm{GE(mag)}}{2.5}} \equiv F_{obs} \cdot F_{ext} \tag{3.8}$$

The error associated to galactic extinction is considered equal to zero, since it's not provided in the NED.

Moreover, the spectroscopic catalogs provided by JADES has fluxes corrected for slit losses only in the case of point-like sources. Since our targets are extended sources, we have to apply **slit losses correction** on Hα and Hβ emission lines fluxes. Because of slit-based measurements, a fraction of the galaxy's flux falls outside the slit aperture, leading to systematically lower fluxes in the spectra compared to the corresponding photometric measurements.

The slit loss correction for the targets in our sample is derived from the work of Pietro Benotto and is estimated as follows: first, the photometric bandpasses are convolved with the observed spectra to estimate the amount of spectral flux that would be detected if the observation were made through the corresponding photometric filter. Next, the ratio between the photometric and spectroscopic flux is computed for each band. Finally, a linear fit of the ratio values provides the best-fit line, which can be used to correct the fluxes according to the equation 3.9:

$$F_{corr,\mathrm{SLIT}} = F_{obs} \cdot [m \cdot \lambda_{obs}(\text{Å}) + q] \equiv F_{obs} \cdot F_{slit} \tag{3.9}$$

where m and q are the angular coefficient and intercept of the best fit line.

The error associated to slit loss correction is:

$$\begin{aligned}\sigma^2_{slit} &= \left(\frac{\partial F_{slit}}{\partial m}\right)^2 \sigma^2_m + \left(\frac{\partial F_{slit}}{\partial q}\right)^2 \sigma^2_q + 2\left(\frac{\partial F_{slit}}{\partial m}\right)\left(\frac{\partial F_{slit}}{\partial q}\right) Cov(m,q) \\ &= \lambda^2\sigma^2_m + \sigma^2_q + 2\lambda Cov(m,q) \end{aligned} \tag{3.10}$$

We could not apply slit losses corrections to all the sample due to continuum spectra missing for some targets. For this reason, the number of targets in the sample decreases to 504.

The final **flux corrected** for both galactic extinction and slit losses effects will be given by equation 3.11:

$$F_{corr} = F_{obs} \cdot F_{ext} \cdot F_{slit} \equiv F_{obs} \cdot 10^{(\frac{\mathrm{GE}}{2.5})} \cdot [m \cdot \lambda_{obs}(\text{Å}) + q] \tag{3.11}$$

The associated error will be:

$$\begin{aligned}\sigma^2_{corr} &= \left(\frac{\partial F_{corr}}{\partial F_{obs}}\right)^2 \sigma^2_{obs} + \left(\frac{\partial F_{corr}}{\partial F_{ext}}\right)^2 \sigma^2_{ext} + \left(\frac{\partial F_{corr}}{\partial F_{slit}}\right)^2 \sigma^2_{slit} \\ &= (F_{ext} \cdot F_{slit})^2 \cdot \sigma^2_{obs} + (F_{obs} \cdot F_{ext})^2 \cdot \sigma^2_{slit} \\ &= (F_{obs} \cdot [m \cdot \lambda + q])^2 \sigma^2_{obs} + (F_{obs} \cdot 10^{(\frac{\mathrm{GE}}{2.5})})^2 \sigma^2_{slit} \end{aligned} \tag{3.12}$$

with:

$$\sigma^2_{slit} = \lambda^2\sigma^2_m + \sigma^2_q + 2\lambda Cov(m,q) \tag{3.13}$$

These corrections have been applied to both emission line fluxes and 1D prism continuum spectra provided by JADES.

3.4 Balmer Optical Depth Computation

We computed the Balmer optical depth τ^l_B using the equation (1.20). We used the emission lines fluxes of Hα and Hβ provided by the JADES catalog and corrected for galactic extinction and slit loss effects according to equation 3.11, with corresponding errors $\sigma_{F\alpha}$ and $\sigma_{F\beta}$ estimated with the formula 3.12. The error associated to the Balmer optical depth is:

$$\sigma_{\tau^l_B} = \sqrt{\left(\frac{\partial \tau}{\partial F\alpha}\right)^2 \sigma^2_{F\alpha} + \left(\frac{\partial \tau}{\partial F\beta}\right)^2 \sigma^2_{F\beta}} = \sqrt{\left(\frac{\sigma_{F\alpha}}{F\alpha}\right)^2 + \left(\frac{\sigma_{F\beta}}{F\beta}\right)^2} \tag{3.14}$$

This error is a bit overestimated because we did not consider the intrinsic correlation between Hα and Hβ emissions which emerges in the estimation of the intercept and slope coefficient in the linear fit procedure described in Section 3.3.

3.5 Average SEDs Derivation

In order to study the average spectral energy distribution in different bins of Balmer optical depth τ_B^l we used the 1d prism continuum spectra provided by JADES. Specifically, we use the low-resolution spectra because the continuum is not detected in the high-resolution spectra. In the latter, the flux is distributed over more channels, requiring much longer integration times. Emission lines, on the other hand, are easier to detect as they are much brighter. Before computing the average SEDs in each τ_B^l bin, since our targets span different redshifts with $1.87 \lesssim z \lesssim 6.81$, and we are interested in the spectral continuum features, several operations on the prism spectra have been performed. The order of operations is as follows:

1. Removal of Nan and negative values of the fluxes;
2. Shift of the observed spectra of each target to the rest-frame with the inverse of relation (2.1);
3. Removal of emission lines by using masks at the location of expected emissions, and a linear interpolation that keeps the same number of points of the original spectra. The size ϵ chosen for the masks interval is 0.001 μm, but a bigger interval was set for more evident and wider emission lines, like OIII ($\epsilon = 0.03$ μm), SIII ($\epsilon = 0.03$ μm), and NeIII ($\epsilon = 0.013$ μm);
4. Selection of the wavelength range common to all targets, since according to the redshift they will lie in different wavalength intervals;
5. Regridding to bring all the spectra to the same resolution: the effect of redshift is also to narrow the width of the wavelength intervals, so that the spectra will have different resolution in the common region selected in point (3). The resolution corresponding to the spectrum with the lowest resolution in the entire sample was chosen.
6. Normalization of the spectra by the flux value at 5500Å;

After the initial spectral processing, the spectra were prepared for stacking. For each τ_B^l bin, an average spectrum was computed, along with the corresponding dispersion within the stack. To extend the wavelength coverage of the attenuation curve, this procedure was applied separately to three distinct spectral regions, which were then combined into a single, continuous average SED. A final smoothing step was performed using a median filter with a kernel size of 11 points, aimed at better highlighting the shape of the continuum. The results are discussed in Section 4.3.

Chapter 4

Dust Attenuation Curve

Our aim is to characterize the dust attenuation curve for high redshift galaxies. The dust attenuation curve describes how the value of the optical depth $\tau(\lambda)$ varies with wavelength λ, showing how the medium absorbs and scatters light at different wavelengths.
As explained in Section 1.2.1 it is difficult to determine the optical depth of a galaxy, in which the intrinsic SED is significantly influenced by multiple factors.

As a first attempt for deriving an attenuation curve, we work under the assumption that the average flux density of the spectra within all bins of the same Balmer optical depth τ_B^l create template spectra which represent galaxies with the same average stellar population age, in order to isolate and highlight the effect of dust on the observed spectra. However, if galaxies actually have very different stellar ages within the same bin of τ_B^l, the assumption may not be valid and could introduce errors in the derivation of the attenuation curve.
In the context of galaxies we can derive the so-called selective attenuation curve $Q_{n,r}(\lambda)$, obtained by comparing the average SEDs of galaxies binned according to τ_B^l, as we will explain in Section 4.3.

In this chapter we describe the physical properties of the sample (Section 4.1); show and discuss the relation between the Balmer optical depth τ_B^l and the UV-β slope (Section 4.2); show the average SEDs obtained in each bin of τ_B^l and the derived selective attenuation curve 4.3; in the end (Section 4.4) we have searched for possible evidence of redshift evolution of the dust attenuation curve.

4.1 Physical Parameters of the Galaxy Sample

The galaxy sample, selected through several steps summarized in Table 2.1, spans a redshift range of $1.87 < z < 6.81$. The redshift distribution is shown in Figure 4.1: lower-redshift bins are more populated than the higher-redshift ones, likely due to selection effects related to the telescope's sensitivity and to the selection function of the JADES targets.

We estimated stellar masses, M_*, and specific star formation rates, sSFR, using `BAGPIPES`. The range of stellar masses is $7.20 < \log(M_*/M_\odot) < 11.07$. In Figure 4.2, we show the distribution of stellar masses as a function of redshift to assess the statistical representativeness of our sample. The distribution shows no clear increase in the stellar mass detection limit with redshift, as low-mass galaxies ($\log(M_*/M_\odot) < 9$) are observed up to $z \sim 6$. Across the redshift range, the sample spans a broad range of stellar masses. Massive galaxies with

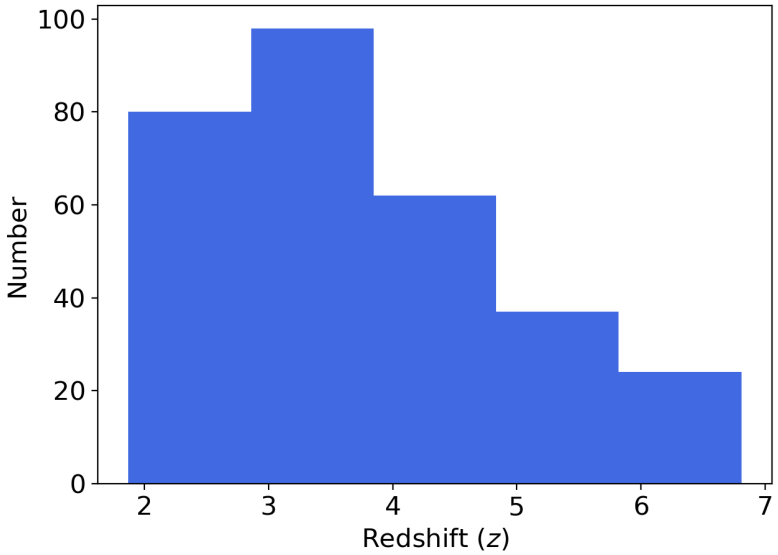

Figure 4.1: Redshift distribution of sources in the selected sample.

$\log(M_*/M_\odot) \geq 10.5$ are only found at lower redshifts ($z < 4$), but aside from this, the stellar mass coverage remains broadly uniform.

The range of sSFR spans $-8.94 < \log(\mathrm{sSFR/yr^{-1}}) < -7.93$, including one source with a notably lower value of $\log(\mathrm{sSFR/yr^{-1}}) \sim -9.63$, which lies outside the main distribution, as shown in Figure 4.3. As a first attempt to derive sSFRs, we adopted a delayed-τ SFH in our SED fitting. While this model captures a range of realistic galaxy evolutionary paths, it assumes a smooth and monotonic decline in star formation, potentially underestimating the diversity of recent star formation episodes—particularly in systems with rising or bursty SFHs. If more flexible or non-parametric SFHs were adopted, one would expect increased scatter in the derived sSFRs, especially at the high end, where recent starbursts could be more accurately captured. The average sSFR across the sample might also be slightly over- or underestimated, depending on how the true SFHs of individual galaxies deviate from the assumed model.
However, since our primary aim is to investigate trends in the average dust attenuation curve, the use of a consistent SFH model across the entire sample (such as the delayed-τ) ensures relative consistency among sSFR estimates. Although the absolute values of sSFR may be slightly over- or underestimated, this systematic effect applies uniformly across the sample and therefore would not significantly impact the relative trends.

As explained in Sections 3.2 and 3.4, we computed the β and τ_B^l parameters, which trace the dust content affecting the stellar continuum and the emission lines from ionized regions, respectively. Stellar mass is plotted as a function of τ_B^l (left) and β (right) in Figure 4.4. As shown in the first panel, more massive galaxies tend to contain more dust, as indicated by the increasing trend of stellar mass with τ_B^l. A similar correlation is observed in the second panel, which illustrates the dependence on β. Therefore, in addition to τ_B^l, β can be considered, to first order, a dust tracer—although with greater interpretative challenges due to its sensitivity to variations in the stellar population. In Section 4.2 we study the $\beta - \tau_B^l$ relation on which is based the method according to Calzetti et al. (1994).

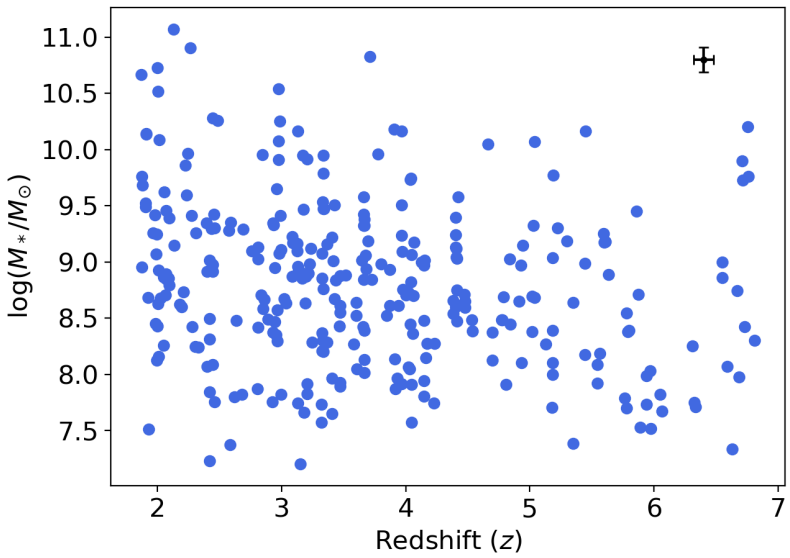

Figure 4.2: Distribution of stellar masses as a function of redshift. The black error bars indicate the typical uncertainties on both axes.

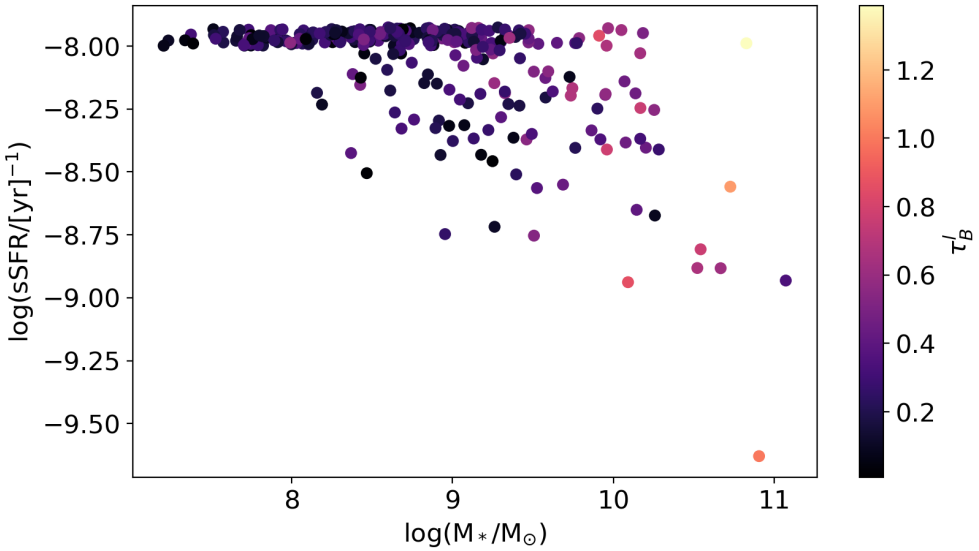

Figure 4.3: sSFR as function of stellar masses M_* and colorbar referred to Balmer optical depth τ_B^l.

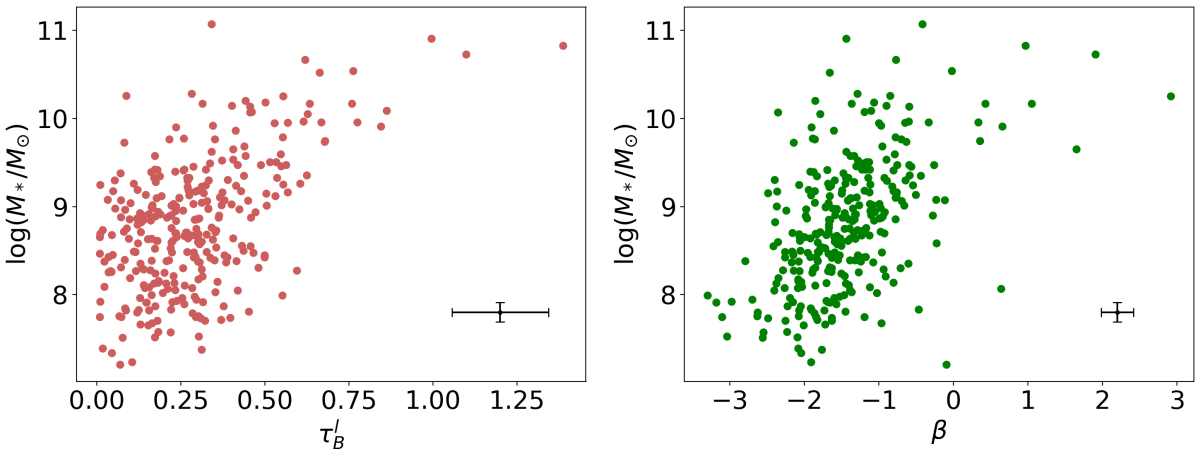

Figure 4.4: Stellar mass distribution as function of the Balmer optical depth τ_B^l in the first panel, and β in the second panel. The black error bars indicate the typical uncertainties on both axes.

4.2 $\beta - \tau_B^l$ Relation

We analyze the $\beta - \tau_B^l$ relation and compare it to the relation found in the Local Universe ($z \lesssim 0.1$) by Battisti et al. (2016). Since the UV slope β and the Balmer optical depth τ_B^l are two indicators of the dust content of galaxies we expect a linear and positive correlation between them. We plotted them into a scatter plot, with a color-bar referred to the redshift of each target. Then, we performed a weighted linear fit by using the package `linmix`, taking into account the intrinsic scattering of the relation.
In the fit performance we included target with $\tau_B^l < 0$, but compatible with the zero within the error bars. Since the $\beta - \tau_B^l$ relation is intrinsically much scattered, we preferred to maximize the available statistics as much as possible.
We include in the analysis those targets whose errors on β and τ_B^l exceed the measured values, since β can assume negative values by definition and there is no physical justification for imposing a cutoff. Also, as explained in Section 3.4, the errors on τ_B^l are likely overestimated. In addition, the fit is weighted on the error, so these targets should not cause a big problem in the final relation. The result is shown in Figure 4.5.

We can see the expected linear and positive relationship between β and τ_B^l, which indicates that the dust behaves as a foreground-like screen to ionized gas region: in this scenario the reddening of the stellar continuum linearly correlates with the reddening of nebular regions. But the correlation is not significant: a large degree of scatter is present in the $\beta - \tau_B^l$ plane. The reason is to be found in the fact that β tends to be more dependent on variations in the age of the stellar population, the star formation history, and/or the metallicity of each galaxy, according to Calzetti et al. (1994). Moreover, since the scatter appears to be fairly uniform across all values of τ_B^l, we can exclude variations in dust geometry as the primary cause of this dispersion. If dust geometry were the main driver, we would expect the scatter to decrease as $\tau_B^l \to 0$.
The red line in Figure 4.5 is the linear fit performed using `linmix`. We found a relation:

$$\beta = (1.93 \pm 0.21)\tau_B^l - (1.90 \pm 0.07) \tag{4.1}$$

In the end, we searched for a possible redshift evolution of the slope, by using a color-bar in the scatter plot. However, by visual inspection, we do not notice a clear dependence

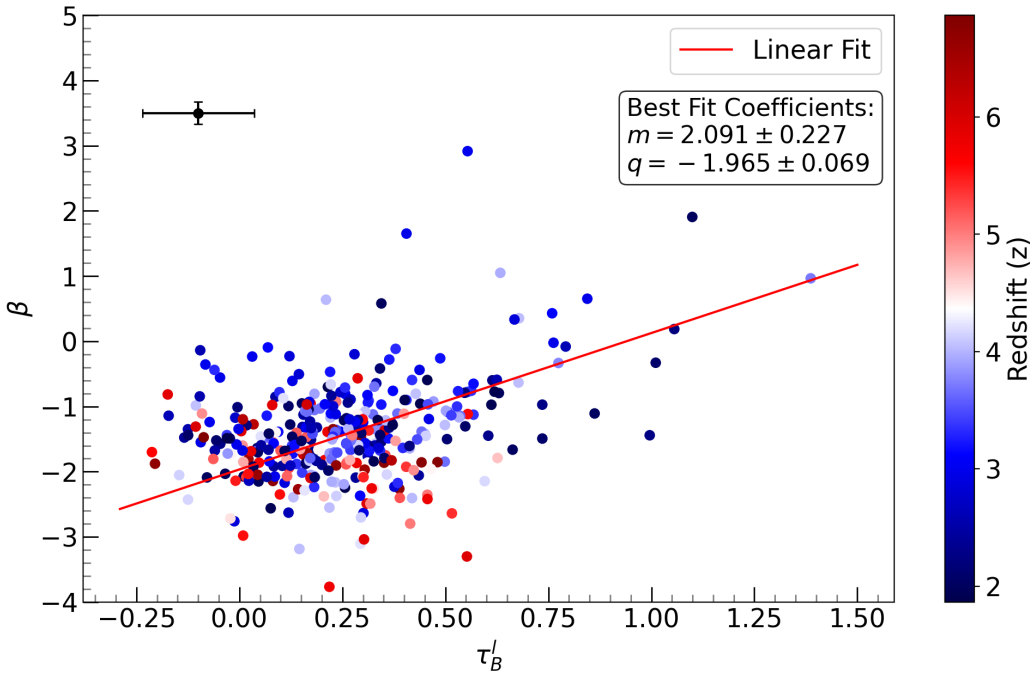

Figure 4.5: Scatter plot of the $\beta - \tau_B^l$ relationship. The color-bar represents the redshift z of each target; the black error-bar represents the mean error on the parameters β and τ_B^l; the red line is the linear fit performed using `linmix`.

on the redshift, only that some higher redshift targets tends to have smaller β value with respect to the lowest redshift galaxies. Nonetheless, it should be verified whether this is not a selection effect, since we tend to observe brighter objects at higher redshifts, which may exhibit lower β values.
For this reason we decided to include all the redshifts in our analysis, without performing a bin in redshift.

4.3 Selective Attenuation Curve

We have divided the sample in stellar mass bins in order to separate the more massive $\log(M/M_\odot) \geq 9$, and therefore more extinguished, galaxies from the less massive ones. The ideal case would have been to separate the low masses from the intermediate ones and from the very massive ones, but the mass bin with $\log(M/M_\odot) \geq 10$ has too low statistics to be taken into consideration.
Therefore, in order to ensure a statistically significant sample we considered two bins, as shown in Figure 4.6.

Subsequently, the distribution of the Balmer optical depth τ_B^l within each mass bin was studied. A binning in τ_B^l was then performed to obtain the average SEDs within each bin. However, since low-mass galaxies are fainter and exhibit lower SNR in the continuum, we were uncertain about the reliability of their spectral shapes. Therefore, we chose to focus our analysis on the high-mass bin, where extinction effects are also more pronounced.
Within the subsample of more massive galaxies, the Balmer optical depth spans the range $0 \leq \tau_B^l \leq 1.39$. However, a cut at $\tau_B^l \leq 0.9$ was applied, since only three objects exceed this value. Including them would have required a bin that was both too wide and poorly

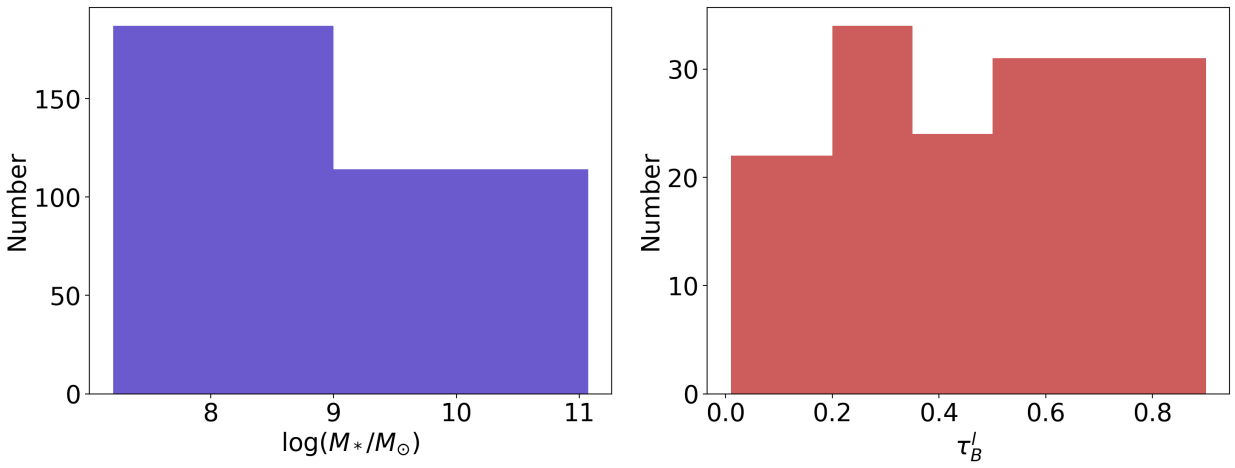

Figure 4.6: Mass distribution in the left panel; τ_B^l distribution within the mass subsample with $\log(M_*/M_\odot) \geq 9$.

populated. Moreover, the limited number of high-τ_B^l sources prevents the creation of additional well-sampled bins in that regime. The final binning scheme adopted for τ_B^l is shown in Figure 4.6.

For each τ_B^l bin, we constructed the average SEDs following the procedure described in Section 3.5. This procedure was applied to three distinct spectral regions. In particular, the central interval, 0.21 μm $\lesssim \lambda \lesssim$ 0.68 μm, corresponds to the rest-frame range common to all targets and thus provides the highest statistical reliability. The number of objects contributing to this interval in each τ_B^l bin is shown in Figure 4.6. The outer regions of the templates are also well sampled, with each including more than 50% of the total sample. This resulted in four average spectral templates spanning the wavelength range 0.16 μm $\lesssim \lambda \lesssim$ 1.14 μm. In Figure 4.7 we show the distributions of redshift, Balmer optical depth, and specific star formation rate for each subsample defined by the τ_B^l binning. The redshift distribution is well sampled up to $z \lesssim 4$ in all bins. At higher redshifts, the sampling becomes less uniform; however, as discussed in Section 4.2, this does not bias our analysis, since the β–τ_B^l relation shows no significant dependence on redshift. For this reason, we chose not to impose a redshift cut at $z < 4$. The τ_B^l distributions appear fairly uniform across the bins, with the exception of the $0.5 < \tau_B^l < 0.9$ bin, which is less populated. However, this does not affect the construction of the dust attenuation curve, as each SED ratio is normalized using the median τ_B^l value of the corresponding bin, as described in the following section. The sSFR distributions indicate that the targets exhibit, on average, similar star formation properties, with all τ_B^l bins peaking around $\log(\text{sSFR}) \sim -8.0$.
In Figure 4.8 we show the average SEDs in each τ_B^l bin.

We observe an increase in attenuation in the average spectra with increasing τ_B^l, as indicated by the flattening of the UV slope. The attenuation is more pronounced at lower wavelengths as expected. There is no clear evidence of the 2175 Å spectral bump, likely due to its weak statistical significance, which causes it to be averaged out during the construction of the average SED templates.
The templates show a similar Balmer break around 4000 Å —clearly smoothed out by the spectral resolution— indicating roughly similar stellar populations. This implies that the different trends in the UV dictated primarly by differencies in dust obscuration, as parametrized by τ_b and not by significant differencies in the average intrinsic stellar popula-

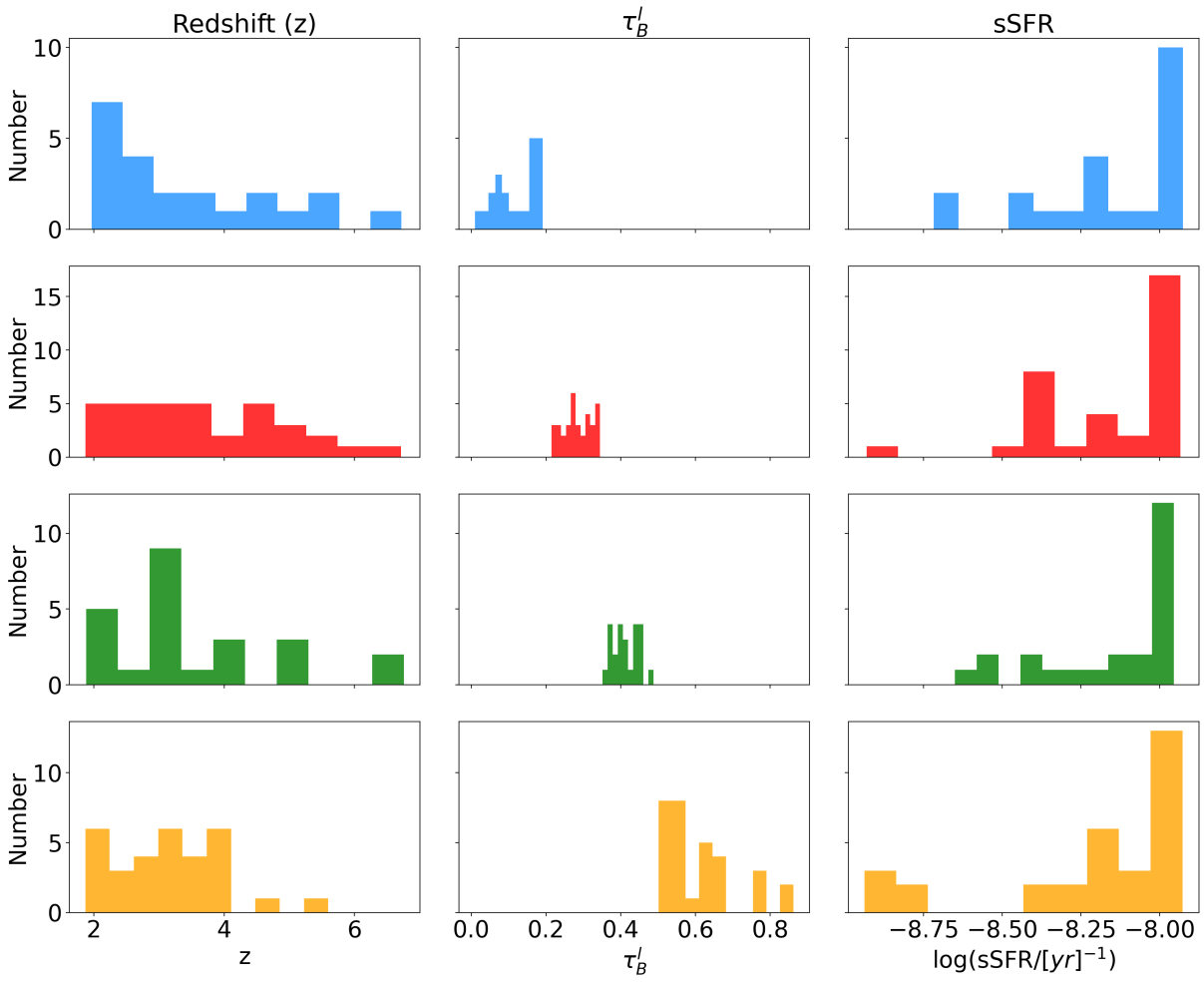

Figure 4.7: From left to right: redshift (z), τ_B^l and sSFR distribution in each τ_B^l bin.

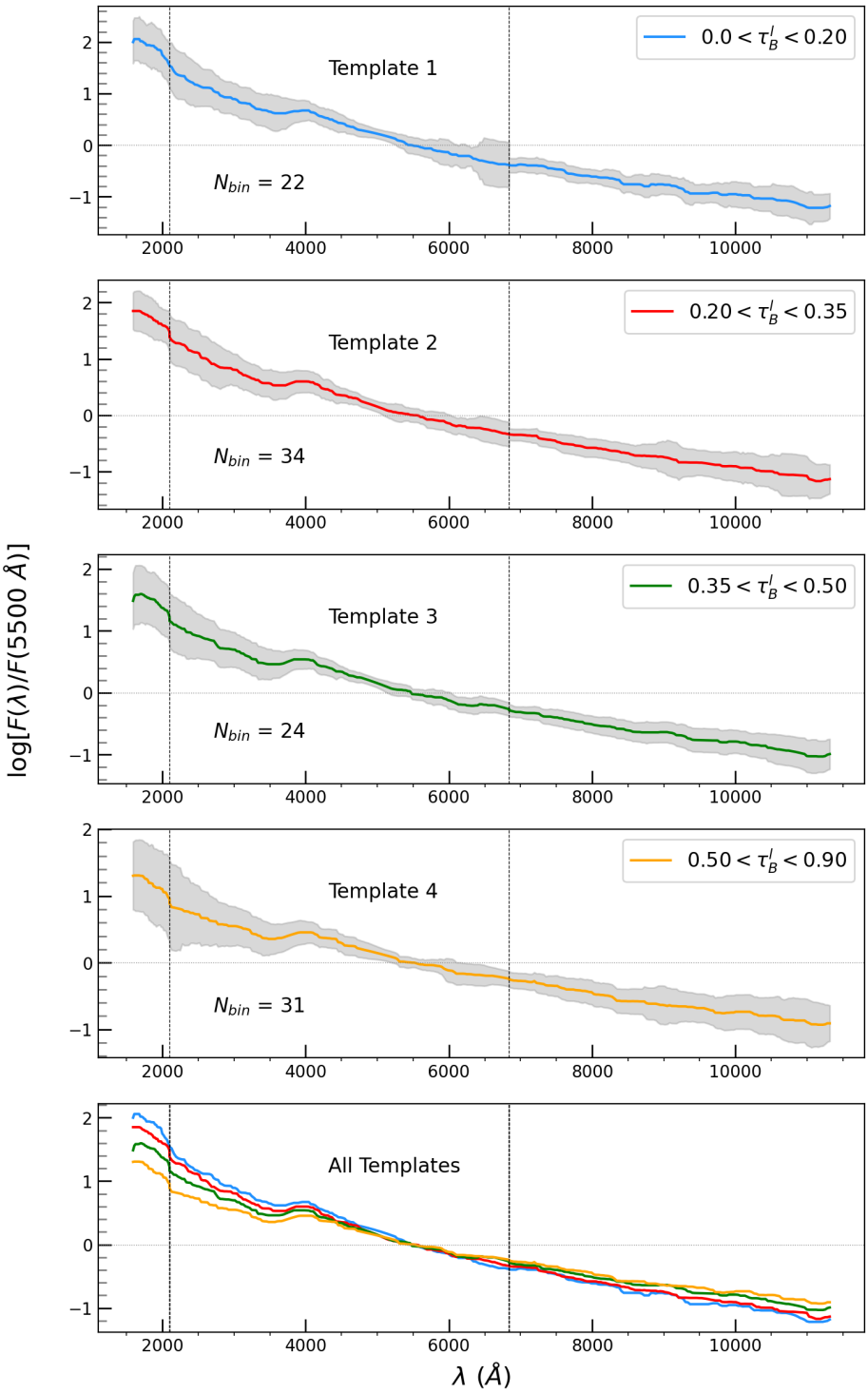

Figure 4.8: Average spectral energy distributions (SEDs) in τ_B^l bins. The vertical dotted lines delimit the central wavelength range that is common to all targets in the sample; the number of spectra contributing to each bin within this region is indicated. The outer regions correspond to wavelengths covered by more than 50% of the sources.

tions from one τ_B^l bin to another. This is also confirmed by the fact that each τ_B^l bin, shows similar average sSFR. As consequence, the shape of the selective attenuation templates Q_i will probe directly the wavelength dependence of dust attenuation.

Once computed the four average SEDs in bin of τ_B^l, we derived the templates for the selective attenuation curve $Q_{n,r}(\lambda)$, given all the possible combination of the templates as explained in Section 4.3. Given a spectrum n, and a reference spectrum r, with $r < n$, all the possible combination of their ratio are: $Q_{2,1}$, $Q_{3,1}$, $Q_{4,1}$, $Q_{3,2}$, $Q_{4,2}$ and $Q_{4,3}$.
Each combined SED ratio was normalized by the difference in the median Balmer optical depth between templates n and r, following Equation 1.25.
We stress that since the templates are spectral averages of different galaxies, i.e. at different distances (redshift), the quantity (1.23) give us informations on the *selective* attenuation, but not a *total* attenuation, and because of this the zero-point of $Q_{n,r}(\lambda)$ is arbitrary. Following Calzetti et al. (1994) and Battisti et al. (2016) we select $Q_n(5500\ \mathring{A}) = 0.0$ as the zero-point.

After we have obtained the $Q_{n,r}(\lambda)$ curves, we averaged them to produce the effective extinction law $Q_{\mathit{eff}}(\lambda)$.

Figure 4.9 shows the selective attenuation curves $Q_{n,r}(\lambda)$, along with the effective curve $Q_{\mathit{eff}}(\lambda)$. The $Q_{n,r}(\lambda)$ templates appear quite noisy. Applying a smoothing filter to the individual spectra before stacking would have resulted in smoother average SEDs and, consequently, in less choppy $Q_{n,r}(\lambda)$ curves. Smoothing was intentionally applied only after constructing the average SEDs over the full wavelength coverage—achieved by joining the average SEDs from the three spectral regions described earlier. Smoothing prior to this step would have introduced artificial trends at the junctions between spectral segments. However, the $Q_{eff}(\lambda)$ curve, obtained from the average of $Q_{n,r}(\lambda)$, exhibits a sufficiently smooth and physically consistent trend, ensuring that the subsequent fitting procedure does not introduce artificial oscillations or noise-driven artifacts.

As a final step, we performed a single third-order polynomial fit of $Q_{\mathit{eff}}(\lambda)$ as a function of $x = \lambda(\mu m)$, and compared it to previous works. We obtained the following function:

$$Q_{fit}(x) = 3.265 - 11.111x + 11.861x^2 - 4.555x^3, \qquad 0.159\ \mu m \leq \lambda \leq 1.132\ \mu m \tag{4.2}$$

In Figure 4.10, we show the best fit curve $Q_{fit}(\lambda)$ and the comparison with previous works in both local and distant Universe. We recall that Shivaei et al. (2020), for the high-metallicity curve, and Battisti et al. (2022) found that the attenuation curve is best fitted when including a UV bump at 2175 Å. However, since we did not explicitly investigate the presence of this feature in our analysis, we chose to display only the underlying continuum from their models, excluding the bump contribution.

Our selective attenuation curve in the blue region ($\lambda < 5000$ Å) is consistent with the results of Reddy et al. (2015) at $z \sim 2$ for galaxies with $-8.84 < \log(\mathrm{sSFR}) < -8.0$, and Battisti et al. (2022) at $z \sim 1.4$ and $\log(\mathrm{sSFR}) \sim -8.4$. The galaxies in our sample exhibit sSFR values similar to those in the range considered by Reddy et al. (2015) and Battisti et al. (2022). The works by Calzetti et al. (1994) and Battisti et al. (2016) at $z \sim 0$, Reddy et al. (2015), Shivaei et al. (2020) at $z \sim 2$, with samples that have smaller sSFR than ours, appear steeper in the UV.

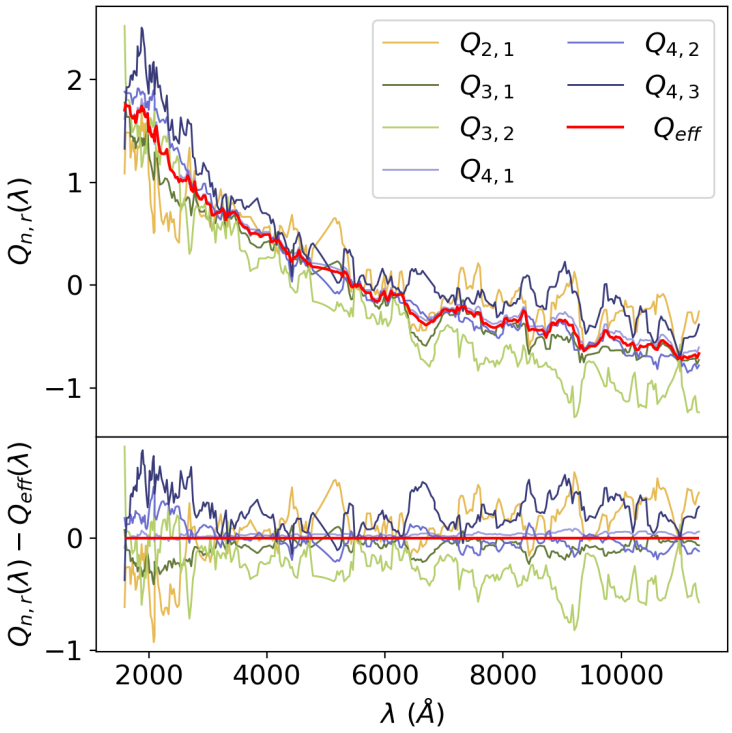

Figure 4.9: Selective attenuation curve templates $Q_{n,r}(\lambda)$ obtained from all possible combinations of SED templates, and the effective attenuation curve $Q_{eff}(\lambda)$ derived as their average (top panel); residuals between each selective attenuation curve $Q_{n,r}(\lambda)$ and the effective curve $Q_{eff}(\lambda)$ (bottom panel).

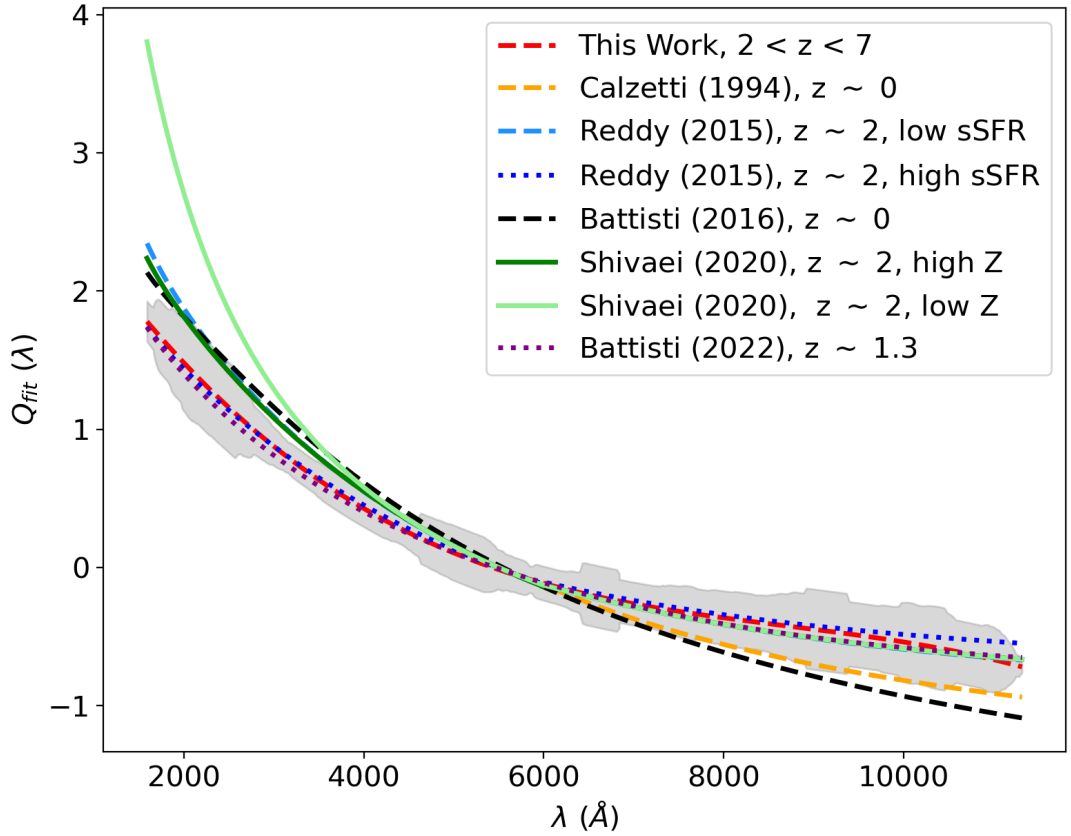

Figure 4.10: Third-order polynomial fit of the effective attenuation curve, $Q_{\rm fit}(\lambda)$ (dashed red line), compared with results from Calzetti et al. (1994) (dashed yellow line), Battisti et al. (2016) (dashed black line), Reddy et al. (2015) divided by sSFR range (dashed light blue and dotted blue lines), Shivaei et al. (2020) divided by metallicity (Z) range (green and light green lines), and Battisti et al. (2022) (dotted purple line). The gray shaded region represents the range of $Q_{n,r}(\lambda)$ values (i.e., the envelope spanned by the curves shown in Figure 1.23).

At longer wavelengths, our curve is compatible with high redshift results ($z > 1$) by Reddy et al. (2015) for both sSFR subsamples, Shivaei et al. (2020) for both metallicity subsamples, and Battisti et al. (2022), independently on sSFR. The observed decline beyond $\lambda > 10000$ Å is likely not physical and may reflect limitations in the data or increased uncertainties in this spectral region. For this reason we do not consider this interval in the following discussion. In contrast, our results show no compatibility with the attenuation curves derived in the local Universe by Calzetti et al. (1994) and Battisti et al. (2016).

These results suggest that dust attenuation in the UV may be correlated with the specific star formation rate of galaxies.

As explained in Section 1.2, in order to obtain the actual selective attenuation on the stellar continuum, we need to introduce the factor f defined in equation 1.30, that takes into account the differential attenuation between ionized gas and stellar continuum. It can be easily calculated imposing the normalization $\mathrm{k(B)} - \mathrm{k(V)} \equiv 1$, with $\mathrm{k}(\lambda)$ total attenuation curve defined by eq. 1.16. In this way, we can write:

$$f = \frac{1}{Q(B) - Q(V)} \tag{4.3}$$

where the B and V bands are assumed to be 4400Å and 5500Å, respectively. We computed $Q(B)$ and $Q(V)$ from equation 4.2. The value of f for our average selective attenuation curve, $Q_{fit}(\lambda)$, is $f = 3.330^{+0.781}_{-0.476}$. The uncertainties reflect the maximum and minimum values of f from fits using individual $Q_{n,r}(\lambda)$. The resulting $fQ_{fit}(\lambda)$ curve, together with previous works results, is shown in Figure 4.11. The values of f in other works are $f = 2.629$ in Calzetti et al. (1994); $f = 2.296$ in Battisti et al. (2016); $f = 2.676$ and $f = 3.178$ for the lower and higher sSFR subsample, respectively, in Reddy et al. (2015); $f = 2.659$ for both metallicity subsamples in Shivaei et al. (2020); and $f = 3.80$ in Battisti et al. (2022).
When introducing the factor f, the slopes of all attenuation curve —excluding the curve at low metallicity by Shivaei et al. (2020)— become strikingly similar. Our curve is consistent with all of them for $\lambda \lesssim 6400$, Å, except for the curve by Battisti et al. (2016), which deviates at $\lambda < 2000$ Å.

This result gives new insights on the physical interpretation of dust obscuration in high redshift galaxies. The dependence of the effective attenuation curve on sSFR is manifested in the degree to which $\mathrm{E(B-V)_{gas}}$ diverges from $\mathrm{E(B-V)_{stars}}$. The differential attenuation between ionized gas and stellar continuum increases with the increase of sSFR. Reddy et al. (2015) found that the correlation between the difference in color excesses of the gas and stellar continuum and the SFR is even stronger than its correlation with the sSFR.
Reddy et al. (2015) proposes a simple two-component stellar population model to explain the observations. The first population, which experiences modest attenuation due to relatively low dust content, dominates the observed UV–optical continuum and is present at all SFR levels. The second population is heavily attenuated, located in very dusty and thus optically thick regions. This component dominates the nebular emission lines and the total bolometric luminosity (including the infrared). Its relative contribution increases with SFR. In other words, as the SFR rises and the ISM becomes more dust-enriched, a larger fraction of stars resides in highly obscured regions, leading to a growing difference between the attenuation of the gas (traced by $\mathrm{H}\alpha/\mathrm{H}\beta$ and strongly attenuated) and that of the stellar continuum (dominated by less obscured stars). This model differs somewhat from those proposed for local galaxies (e.g., Charlot and Fall (2000); Calzetti et al. (1994)), in which young stars are

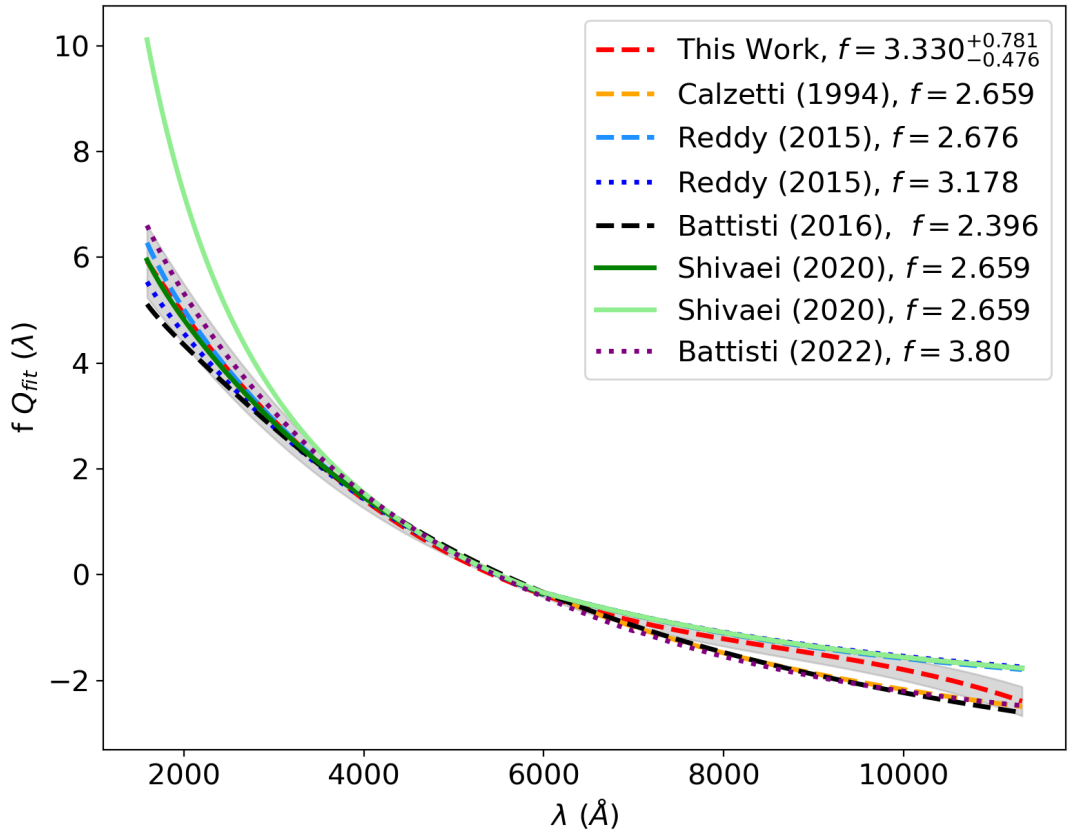

Figure 4.11: Effective attenuation curve on the stellar continuum, $fQ_{\rm fit}(\lambda)$ (dashed red line), compared with results from Calzetti et al. (1994) (dashed yellow line), Battisti et al. (2016) (dashed black line), Reddy et al. (2015) divided by sSFR range (dashed light blue and dotted blue lines), Shivaei et al. (2020) divided by metallicity (Z) range (green and light green lines), and Battisti et al. (2022) (dotted purple line). The gray shaded region reflect the maximum and minimum values of f from fits using individual $Q_{n,r}(\lambda)$.

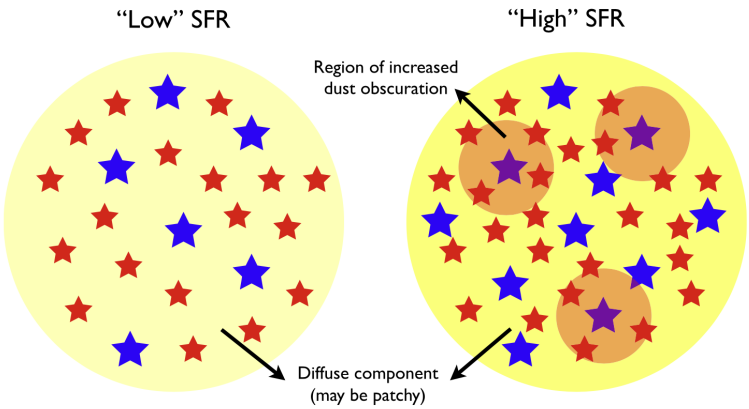

Figure 4.12: Illustration of a simple geometry of dust and gas that can account for the trends in the difference between ionized gas and continuum color excess, and total attenuation, vs. SFR. The yellow region denotes the diffuse dust component (which may be patchy). The red regions indicate areas of increased dustiness within the galaxy. The blue and red stars indicate high mass (ionizing) and lower mass stars, respectively. At lower SFRs ($\lesssim 20\ M_{\odot}\ yr^{-1}$), stars of all masses are uniformly obscured. As the SFR increases, the diffuse component becomes more dust-enriched (as indicated by the darker shade of yellow), while regions of more highly obscured SFR (red regions) become prominent, Reddy et al. (2015).

assumed to be embedded in their birth clouds that later dissipate. In such models, the gas is always more attenuated, as it remains in dust-rich HII regions, resulting in a systematic difference between $E(B-V)_{gas}$ and $E(B-V)_{stars}$ regardless of the SFR. However, at higher redshifts, this systematic offset is not observed across all SFRs; rather, the divergence increases with SFR. A simple sketch of this model is shown in Figure 4.12.

For higher wavelengths ($\lambda > 65000$Å), our curve is compatible with all high-z results and shows no consistency with local results. This implies that the curves at high redshift may have a lower normalization R_V with respect curves of nearby galaxies.

In order to examine a possible effect of redshift evolution on the dust attenuation curve we examined its evolution across redshift in Section 4.4.

4.4 Redshift Evolution

Previous results—such as the redshift independence of the β–τ_B^l relation and the consistency of attenuation curves across different redshifts for galaxies with similar sSFR—suggest that the shape (or "grayness") of the selective attenuation curve depends more strongly on sSFR than on redshift. On the other side, the normalization R_V appears to be dependent on redshift. For these reasons we investigated the redshift evolution of dust attenuation. Specifically, we focused on the rest-frame wavelength range common to all sources ($0.50\ \mu m < \lambda < 0.90\ \mu m$), in order to maximize the sample statistics. We divided the sample into two redshift bins, $1.87 < z < 3.33$ and $3.33 < z < 6.76$ as shown in Figure 4.13. This choice was made to ensure that the two bins contain a similar number of objects.

These two subsamples exhibit comparable sSFR distributions, as displayed in Figure 4.14. Within each redshift bin, we further subdivided the galaxies into three τ_B^l bins, illustrated in Figure 4.14. As a reference for comparison, we also constructed an attenuation curve from the full redshift range, using the same new τ_B^l binning. In this case, since we were working

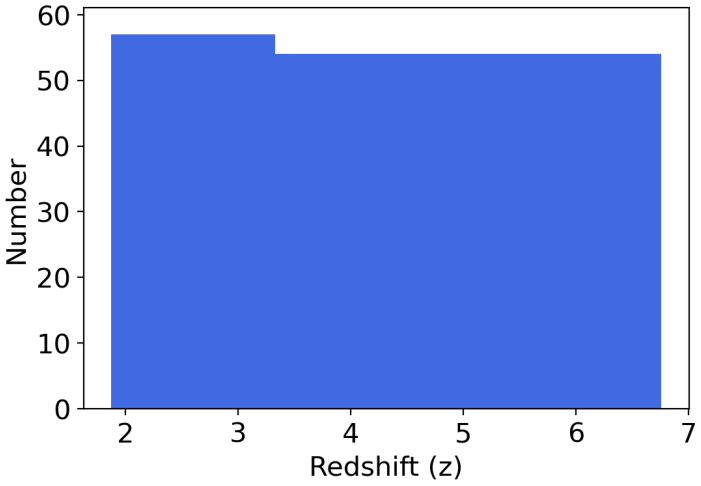

Figure 4.13: Redshift bins dividing the sample into two groups.

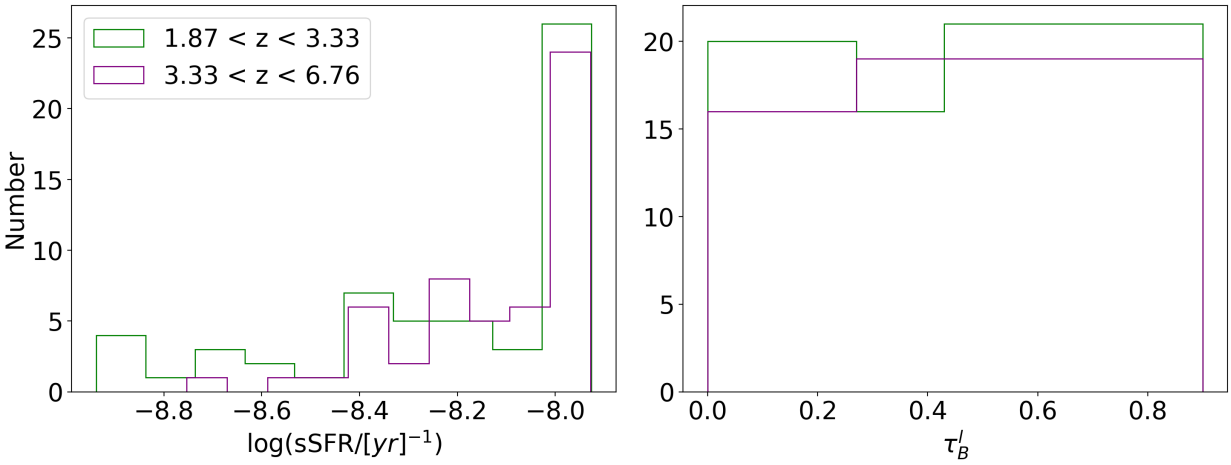

Figure 4.14: sSFR distributions (left panel) and τ_B^l distributions (right panel) in each redshift bin.

within a single wavelength interval, we applied smoothing to the individual spectra before stacking them to create the average SEDs. From these SEDs we derived the $Q_{2,1}$, $Q_{3,1}$, and $Q_{3,2}$ templates, and combined them into the effective attenuation curve $Q_{eff}(\lambda)$. As shown in Figure 4.15, the three curves are consistent with one another, reinforcing the conclusion that the selective attenuation curve does not evolve significantly with redshift.

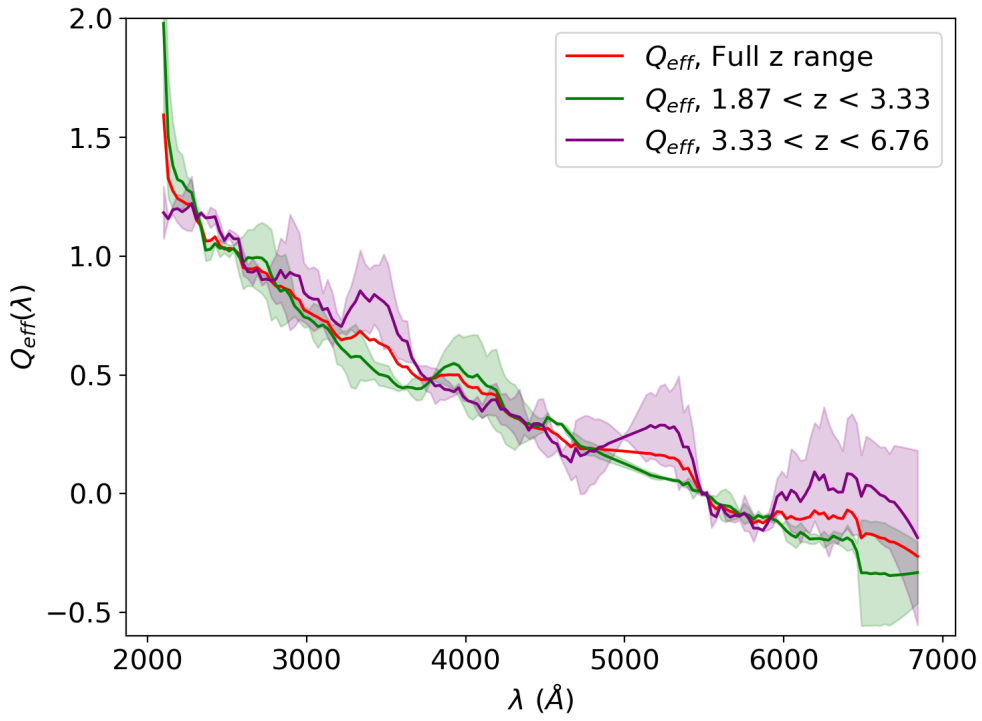

Figure 4.15: Effective attenuation curves $Q_{eff}(\lambda)$ in each redshift bin, with shaded regions indicating the dispersion of $Q_{n,r}(\lambda)$ templates; reference $Q_{eff}(\lambda)$ (red curve) obtained from the sample spanning all redshifts.

Chapter 5

Results and Discussion

In this thesis, we used a sample of 111 star-forming galaxies at redshifts $z = 1.87$–6.76, with measurements of the Hα and Hβ emission lines from JADES DR3, to constrain the dust attenuation curve of high-redshift galaxies by applying the methodology of Calzetti et al. (1994). Our sample spans a stellar mass range of $9 \leq \log(M_*/M_\odot) \leq 11.07$ and a specific star formation rate range of $-8.93 \leq \log(\mathrm{sSFR}/[\mathrm{yr}]^{-1}) \leq -7.93$.

We estimated the UV slope β using ASTRODEEP photometry, and the Balmer optical depth τ_B^l from the Hα and Hβ emission lines provided by JADES DR3. Relying on the linearity of the β–τ_B^l relation, we constructed average SEDs using continuum prism spectra from JADES in bins of τ_B^l, and derived the selective attenuation curve $Q(\lambda)$ from their ratios. Then, we investigated the effects of dust on the stellar continuum of high-redshift galaxies by studying the selective attenuation curve $fQ(\lambda)$, where the factor f accounts for the differential attenuation between nebular emission and stellar continuum, and was derived from the fit of $Q(\lambda)$. In the end, we divided the sample into redshift bins and derived the selective attenuation curve in each bin to search for clues of redshift evolution.

Our $Q(\lambda)$ curve is consistent in the UV with the results of Reddy et al. (2015) and Battisti et al. (2022), whose samples span sSFR ranges similar to ours. In contrast, it differs from studies based on samples with lower sSFRs. At higher wavelengths our curve is compatible with high-redshift works ($z > 1$) by Reddy et al. (2015), Shivaei et al. (2020) and Battisti et al. (2022), whereas it differs from local Universe works by Calzetti et al. (1994) and Battisti et al. (2016).
The $fQ(\lambda)$ curve shows good agreement in the UV with all these studies, except for Battisti et al. (2016) at $\lambda < 2000, \text{Å}$ and the low-metallicity subsample of Shivaei et al. (2020). At longer wavelengths, the discrepancy between local and high-redshift studies persists.
The attenuation curves $Q(\lambda)$ derived in different redshift bins are consistent with each other, suggesting no clear redshift evolution.

These results indicate that UV dust attenuation may correlate with the sSFR of galaxies, such that the differential attenuation between nebular emission and stellar continuum increases with sSFR, while showing no strong dependence on redshift. The only potential redshift dependence of dust attenuation may lie in the normalization factor $\mathrm{R_V}$, as local and high-redshift results differ at longer wavelengths.

The upcoming JADES data release will significantly increase the sample size, allowing us to more robustly test the results presented in this study. In addition, with improved statistics,

it will be possible to define finer bins in stellar mass, sSFR, and redshift, enabling the investigation of potential evolutionary trends in the attenuation curve. Since we are applying this methodology for the first time at very high redshift, using continuum spectra to construct average SEDs, we adopted a conservative approach by relying solely on JADES data. In future work, however, we plan to incorporate data from other high-redshift spectroscopic surveys (e.g., GLASS, FIGS, CEERS, POPPIES, NGSS), which will further increase the sample size and improve the statistical power of the analysis.

Moreover, we aim to include submillimeter observations of JWST targets from ALMA, in order to estimate R_V values where possible. These measurements will provide constraints on the normalization of the attenuation curves and help anchor their absolute scale. Constraining the value of R_V is crucial, as it enables the derivation of the total attenuation curve k_λ and allows for a comprehensive comparison with previous studies. Moreover, it provides the basis for converting to the absolute parametrization A_λ/A_V, where different R_V values result in different curve slopes. This, in turn, allows us to compare our results with model-based works such as Markov et al. (2025), who claim a strong redshift evolution of the dust attenuation curve.

Bibliography

Abazajian, K. N., Adelman-McCarthy, J. K., Agüeros, M. A., Allam, S. S., Allende Prieto, C., An, D., Anderson, K. S. J., Anderson, S. F., Annis, J., Bahcall, N. A., Bailer-Jones, C. A. L., Barentine, J. C., Bassett, B. A., Becker, A. C., Beers, T. C., Bell, E. F., Belokurov, V., Berlind, A. A., Berman, E. F., Bernardi, M., Bickerton, S. J., Bizyaev, D., Blakeslee, J. P., Blanton, M. R., Bochanski, J. J., Boroski, W. N., Brewington, H. J., Brinchmann, J., Brinkmann, J., Brunner, R. J., Budavári, T., Carey, L. N., Carliles, S., Carr, M. A., Castander, F. J., Cinabro, D., Connolly, A. J., Csabai, I., Cunha, C. E., Czarapata, P. C., Davenport, J. R. A., de Haas, E., Dilday, B., Doi, M., Eisenstein, D. J., Evans, M. L., Evans, N. W., Fan, X., Friedman, S. D., Frieman, J. A., Fukugita, M., Gänsicke, B. T., Gates, E., Gillespie, B., Gilmore, G., Gonzalez, B., Gonzalez, C. F., Grebel, E. K., Gunn, J. E., Györy, Z., Hall, P. B., Harding, P., Harris, F. H., Harvanek, M., Hawley, S. L., Hayes, J. J. E., Heckman, T. M., Hendry, J. S., Hennessy, G. S., Hindsley, R. B., Hoblitt, J., Hogan, C. J., Hogg, D. W., Holtzman, J. A., Hyde, J. B., Ichikawa, S.-i., Ichikawa, T., Im, M., Ivezić, Ž., Jester, S., Jiang, L., Johnson, J. A., Jorgensen, A. M., Jurić, M., Kent, S. M., Kessler, R., Kleinman, S. J., Knapp, G. R., Konishi, K., Kron, R. G., Krzesinski, J., Kuropatkin, N., Lampeitl, H., Lebedeva, S., Lee, M. G., Lee, Y. S., French Leger, R., Lépine, S., Li, N., Lima, M., Lin, H., Long, D. C., Loomis, C. P., Loveday, J., Lupton, R. H., Magnier, E., Malanushenko, O., Malanushenko, V., Mandelbaum, R., Margon, B., Marriner, J. P., Martínez-Delgado, D., Matsubara, T., McGehee, P. M., McKay, T. A., Meiksin, A., Morrison, H. L., Mullally, F., Munn, J. A., Murphy, T., Nash, T., Nebot, A., Neilsen, Jr., E. H., Newberg, H. J., Newman, P. R., Nichol, R. C., Nicinski, T., Nieto-Santisteban, M., Nitta, A., Okamura, S., Oravetz, D. J., Ostriker, J. P., Owen, R., Padmanabhan, N., Pan, K., Park, C., Pauls, G., Peoples, Jr., J., Percival, W. J., Pier, J. R., Pope, A. C., Pourbaix, D., Price, P. A., Purger, N., Quinn, T., Raddick, M. J., Re Fiorentin, P., Richards, G. T., Richmond, M. W., Riess, A. G., Rix, H.-W., Rockosi, C. M., Sako, M., Schlegel, D. J., Schneider, D. P., Scholz, R.-D., Schreiber, M. R., Schwope, A. D., Seljak, U., Sesar, B., Sheldon, E., Shimasaku, K., Sibley, V. C., Simmons, A. E., Sivarani, T., Allyn Smith, J., Smith, M. C., Smolčić, V., Snedden, S. A., Stebbins, A., Steinmetz, M., Stoughton, C., Strauss, M. A., SubbaRao, M., Suto, Y., Szalay, A. S., Szapudi, I., Szkody, P., Tanaka, M., Tegmark, M., Teodoro, L. F. A., Thakar, A. R., Tremonti, C. A., Tucker, D. L., Uomoto, A., Vanden Berk, D. E., Vandenberg, J., Vidrih, S., Vogeley, M. S., Voges, W., Vogt, N. P., Wadadekar, Y., Watters, S., Weinberg, D. H., West, A. A., White, S. D. M., Wilhite, B. C., Wonders, A. C., Yanny, B., and Yocum, D. R. (2009). The Seventh Data Release of the Sloan Digital Sky Survey. *Astrophysical Journal Supplement Series*, 182(2):543–558.

Atek, H., Malkan, M., McCarthy, P., Teplitz, H. I., Scarlata, C., Siana, B., Henry, A., Colbert, J. W., Ross, N. R., Bridge, C., Bunker, A. J., Dressler, A., Fosbury, R. A. E.,

Martin, C., and Shim, H. (2010). The WFC3 Infrared Spectroscopic Parallel (WISP) Survey. *The Astrophysical Journal*, 723(1):104–115.

Battisti, A. J., Bagley, M. B., Baronchelli, I., Dai, Y. S., Henry, A. L., Malkan, M. A., Alavi, A., Calzetti, D., Colbert, J., McCarthy, P. J., Mehta, V., Rafelski, M., Scarlata, C., Shivaei, I., and Wisnioski, E. (2022). The average dust attenuation curve at z 1.3 based on hst grism surveys. *Monthly Notices of the Royal Astronomical Society*, 513(3):4431–4450.

Battisti, A. J., Calzetti, D., and Chary, R.-R. (2016). Characterizing dust attenuation in local star-forming galaxies: Uv and optical reddening. *The Astrophysical Journal*, 818(1):13.

Battisti, A. J., Calzetti, D., and Chary, R.-R. (2017). Characterizing dust attenuation in local star-forming galaxies: Inclination effects and the 2175 Å feature. *The Astrophysical Journal*, 851(2):90.

Brammer, G. B., van Dokkum, P. G., Franx, M., Fumagalli, M., Patel, S., Rix, H.-W., Skelton, R. E., Kriek, M., Nelson, E., Schmidt, K. B., Bezanson, R., da Cunha, E., Erb, D. K., Fan, X., Förster Schreiber, N., Illingworth, G. D., Labbé, I., Leja, J., Lundgren, B., Magee, D., Marchesini, D., McCarthy, P., Momcheva, I., Muzzin, A., Quadri, R., Steidel, C. C., Tal, T., Wake, D., Whitaker, K. E., and Williams, A. (2012). 3D-HST: A Wide-field Grism Spectroscopic Survey with the Hubble Space Telescope. *The Astrophysical Journal Supplement Series*, 200(2):13.

Bruzual, G. and Charlot, S. (2003). Stellar population synthesis at the resolution of 2003. *Monthly Notices of the Royal Astronomical Society*, 344(4):1000–1028.

Calzetti, D. (2001). The dust opacity of star-forming galaxies. *Publications of the Astronomical Society of the Pacific*, 113(790):1449.

Calzetti, D., Kinney, A. L., and Storchi-Bergmann, T. (1994). Dust Extinction of the Stellar Continua in Starburst Galaxies: The Ultraviolet and Optical Extinction Law. *The Astrophysical Journal*, 429:582.

Cardelli, J. A., Clayton, G. C., and Mathis, J. S. (1989). The Relationship between Infrared, Optical, and Ultraviolet Extinction. *The Astrophysical Journal*, 345:245.

Carnall, A. C., McLure, R. J., Dunlop, J. S., and Davé, R. (2018). Inferring the star formation histories of massive quiescent galaxies with bagpipes: evidence for multiple quenching mechanisms. *Monthly Notices of the Royal Astronomical Society*, 480(4):4379–4401.

Charlot, S. and Fall, S. M. (2000). A Simple Model for the Absorption of Starlight by Dust in Galaxies. *The Astrophysical Journal*, 539(2):718–731.

Charlot, S. and Longhetti, M. (2001). Nebular emission from star-forming galaxies. *Monthly Notices of the Royal Astronomical Society*, 323(4):887–903.

Chatzikos, M., Bianchi, S., Camilloni, F., Chakraborty, P., Gunasekera, C. M., Guzmán, F., Milby, J. S., Sarkar, A., Shaw, G., van Hoof, P. A., et al. (2023). The 2023 release of cloudy. *Revista mexicana de astronomía y astrofísica*, 59(2):327–343.

da Cunha, E., Charlot, S., and Elbaz, D. (2008). A simple model to interpret the ultraviolet, optical and infrared emission from galaxies. *Monthly Notices of the Royal Astronomical Society*, 388(4):1595–1617.

D'Eugenio, F., Cameron, A. J., Scholtz, J., Carniani, S., Willott, C. J., Curtis-Lake, E., Bunker, A. J., Parlanti, E., Maiolino, R., Willmer, C. N. A., Jakobsen, P., Robertson, B. E., Johnson, B. D., Tacchella, S., Cargile, P. A., Rawle, T., Arribas, S., Chevallard, J., Curti, M., Egami, E., Eisenstein, D. J., Kumari, N., Looser, T. J., Rieke, M. J., Pino, B. R. D., Saxena, A., Übler, H., Venturi, G., Witstok, J., Baker, W. M., Bhatawdekar, R., Bonaventura, N., Boyett, K., Charlot, S., Danhaive, A. L., Hainline, K. N., Hausen, R., Helton, J. M., Ji, X., Ji, Z., Jones, G. C., Joudžbalis, I., Maseda, M. V., Pérez-González, P. G., Perna, M., Puskás, D., Shivaei, I., Silcock, M. S., Simmonds, C., Smit, R., Sun, F., Villanueva, N. C., Williams, C. C., and Zhu, Y. (2024). Jades data release 3 – nirspec/msa spectroscopy for 4,000 galaxies in the goods fields.

Dole, H., Lagache, G., Puget, J.-L., Caputi, K. I., Fernández-Conde, N., Le Floc'h, E., Papovich, C., Pérez-González, P. G., Rieke, G. H., and Blaylock, M. (2006). The cosmic infrared background resolved by spitzer - contributions of mid-infrared galaxies to the far-infrared background. *Astronomy Astrophysics*, 451(2):417–429.

Erb, D. K., Steidel, C. C., Shapley, A. E., Pettini, M., Reddy, N. A., and Adelberger, K. L. (2006). H observations of a large sample of galaxies at z 2: Implications for star formation in high-redshift galaxies*. *The Astrophysical Journal*, 647(1):128.

Ferland, G. J., Fabian, A. C., Hatch, N. A., Johnstone, R. M., Porter, R. L., Van Hoof, P. A. M., and Williams, R. J. R. (2009). Collisional heating as the origin of filament emission in galaxy clusters*. *Monthly Notices of the Royal Astronomical Society*, 392(4):1475–1502.

Feroz, F. and Hobson, M. P. (2008). Multimodal nested sampling: an efficient and robust alternative to Markov Chain Monte Carlo methods for astronomical data analyses. *Monthly Notices of the Royal Astronomical Society*, 384(2):449–463.

Feroz, F., Hobson, M. P., and Bridges, M. (2009). MULTINEST: an efficient and robust Bayesian inference tool for cosmology and particle physics. *Monthly Notices of the Royal Astronomical Society*, 398(4):1601–1614.

Förster Schreiber, N. M., Genzel, R., Bouché, N., Cresci, G., Davies, R., Buschkamp, P., Shapiro, K., Tacconi, L. J., Hicks, E. K. S., Genel, S., Shapley, A. E., Erb, D. K., Steidel, C. C., Lutz, D., Eisenhauer, F., Gillessen, S., Sternberg, A., Renzini, A., Cimatti, A., Daddi, E., Kurk, J., Lilly, S., Kong, X., Lehnert, M. D., Nesvadba, N., Verma, A., McCracken, H., Arimoto, N., Mignoli, M., and Onodera, M. (2009). The SINS Survey: SINFONI Integral Field Spectroscopy of z ~2 Star-forming Galaxies. *The Astrophysical Journal*, 706(2):1364–1428.

Inoue, A. K. (2005). Attenuation law of normal disc galaxies with clumpy distributions of stars and dust. *Monthly Notices of the Royal Astronomical Society*, 359(1):171–182.

Inoue, A. K. (2011). The origin of dust in galaxies revisited: the mechanism determining dust content. *Earth, Planets and Space*, 63(10):1027–1039.

Iyer, K. G., Pacifici, C., Calistro-Rivera, G., and Lovell, C. C. (2025). The Spectral Energy Distributions of Galaxies. *arXiv e-prints*, page arXiv:2502.17680.

Kewley, L. J., Nicholls, D. C., and Sutherland, R. S. (2019). Understanding Galaxy Evolution Through Emission Lines. *Annual Review of Astronomy and Astrophysics*, 57:511–570.

Kriek, M. and Conroy, C. (2013). The dust attenuation law in distant galaxies: Evidence for variation with spectral type. *The Astrophysical Journal*, 775(1):L16.

Kriek, M., Shapley, A. E., Reddy, N. A., Siana, B., Coil, A. L., Mobasher, B., Freeman, W. R., de Groot, L., Price, S. H., Sanders, R., Shivaei, I., Brammer, G. B., Momcheva, I. G., Skelton, R. E., van Dokkum, P. G., Whitaker, K. E., Aird, J., Azadi, M., Kassis, M., Bullock, J. S., Conroy, C., Davé, R., Kereš, D., and Krumholz, M. (2015). The MOSFIRE Deep Evolution Field (MOSDEF) Survey: Rest-frame Optical Spectroscopy for ~1500 H-selected Galaxies at 1.37 ¡ z ¡ 3.8. *The Astrophysical Journal Supplement Series*, 218(2):15.

Li, A. and Draine, B. T. (2001). Infrared Emission from Interstellar Dust. II. The Diffuse Interstellar Medium. *The Astrophysical Journal*, 554(2):778–802.

Lu, K.-X., Zhao, Y., Bai, J.-M., and Fan, X.-L. (2018). Reddening of the blr and nlr in agns from a systematic analysis of balmer decrement. *Monthly Notices of the Royal Astronomical Society*, 483(2):1722–1730.

Maiolino, Scholtz, Jan, Curtis-Lake, Emma, Carniani, Stefano, Baker, William, de Graaff, Anna, Tacchella, Sandro, Übler, Hannah, D'Eugenio, Francesco, Witstok, Joris, Curti, Mirko, Arribas, Santiago, Bunker, Andrew J., Charlot, Stéphane, Chevallard, Jacopo, Eisenstein, Daniel J., Egami, Eiichi, Ji, Zhiyuan, Jones, Gareth C., Lyu, Jianwei, Rawle, Tim, Robertson, Brant, Rujopakarn, Wiphu, Perna, Michele, Sun, Fengwu, Venturi, Giacomo, Williams, Christina C., and Willott, Chris (2024). Jades - the diverse population of infant black holes at 4 ¡ z ¡ 11: Merging, tiny, poor, but mighty. *Astronomy Astrophysics*, 691:A145.

Markov, V., Gallerani, S., Ferrara, A., Pallottini, A., Parlanti, E., Mascia, F. D., Sommovigo, L., and Kohandel, M. (2024). The evolution of dust attenuation in z2–12 galaxies observed by jwst. *Nature Astronomy*, 9(3):458–468.

Markov, V., Gallerani, S., Pallottini, A., Bradac, M., Carniani, S., Tripodi, R., Noirot, G., Mascia, F. D., Parlanti, E., and Martis, N. (2025). Unveiling the trends between dust attenuation and galaxy properties at $z \sim$ 2-12 with jwst.

Martin, D. C., Fanson, J., Schiminovich, D., Morrissey, P., Friedman, P. G., Barlow, T. A., Conrow, T., Grange, R., Jelinsky, P. N., Milliard, B., Siegmund, O. H. W., Bianchi, L., Byun, Y.-I., Donas, J., Forster, K., Heckman, T. M., Lee, Y.-W., Madore, B. F., Malina, R. F., Neff, S. G., Rich, R. M., Small, T., Surber, F., Szalay, A. S., Welsh, B., and Wyder, T. K. (2005). The Galaxy Evolution Explorer: A Space Ultraviolet Survey Mission. *The Astrophysical Journal Letters*, 619(1):L1–L6.

McKee, C. F. and Ostriker, J. P. (1977). A theory of the interstellar medium: three components regulated by supernova explosions in an inhomogeneous substrate. *The Astrophysical Journal*, 218:148–169.

Mclean, I., Steidel, C., Epps, H., Matthews, K., Adkins, S., Konidaris, N., Weber, B., Aliado, T., Brims, G., Canfield, J., Cromer, J., Fucik, J., Kulas, K., Mace, G., Magnone, K., Rodriguez, H., Wang, E., Weiss, J., and Keck, W. (2010). Design and development of mosfire, the multi-object spectrometer for infra-red exploration at the keck observatory. *Proceedings of SPIE*, 7735:77351–77351.

Merlin, E., Santini, P., Paris, D., Castellano, M., Fontana, A., Treu, T., Finkelstein, S. L., Dunlop, J. S., Arrabal Haro, P., Bagley, M., Boyett, K., Calabrò, A., Correnti, M., Davis, K., Dickinson, M., Donnan, C. T., Ferguson, H. C., Fortuni, F., Giavalisco, M., Glazebrook, K., Grazian, A., Grogin, N. A., Hathi, N., Hirschmann, M., Kartaltepe,

J. S., Kewley, L. J., Kirkpatrick, A., Kocevski, D. D., Koekemoer, A. M., Leung, G., Lotz, J. M., Lucas, R. A., Magee, D. K., Marchesini, D., Mascia, S., McLeod, D. J., McLure, R. J., Nanayakkara, T., Napolitano, L., Nonino, M., Papovich, C., Pentericci, L., Pérez-González, P. G., Pirzkal, N., Ravindranath, S., Roberts-Borsani, G., Somerville, R. S., Trenti, M., Trump, J. R., Vulcani, B., Wang, X., Watson, P. J., Wilkins, S. M., Yang, G., and Yung, L. Y. A. (2024). Astrodeep-jwst: Nircam-hst multi-band photometry and redshifts for half a million sources in six extragalactic deep fields. *Astronomy amp; Astrophysics*, 691:A240.

Noll, S., Burgarella, D., Giovannoli, E., Buat, V., Marcillac, D., and Muñoz-Mateos, J. C. (2009). Analysis of galaxy spectral energy distributions from far-UV to far-IR with CIGALE: studying a SINGS test sample. *Astronomy Astrophysics*, 507(3):1793–1813.

Osterbrock, D. E. and Ferland, G. J. (2006). *Astrophysics Of Gas Nebulae and Active Galactic Nuclei*. University science books.

Price, S. H., Kriek, M., Brammer, G. B., Conroy, C., Schreiber, N. M. F., Franx, M., Fumagalli, M., Lundgren, B., Momcheva, I., Nelson, E. J., Skelton, R. E., van Dokkum, P. G., Whitaker, K. E., and Wuyts, S. (2014). Direct measurements of dust attenuation in z 1.5 star-forming galaxies from 3d-hst: Implications for dust geometry and star formation rates. *The Astrophysical Journal*, 788(1):86.

Puglisi, A., Rodighiero, G., Franceschini, A., Talia, M., Cimatti, A., Baronchelli, I., Daddi, E., Renzini, A., Schawinski, K., Mancini, C., Silverman, J., Gruppioni, C., Lutz, D., Berta, S., and Oliver, S. J. (2016). Dust attenuation in z 1 galaxies from herschel and 3d-hst h measurements. *Astronomy Astrophysics*, 586:A83.

Reddy, N. A., Kriek, M., Shapley, A. E., Freeman, W. R., Siana, B., Coil, A. L., Mobasher, B., Price, S. H., Sanders, R. L., and Shivaei, I. (2015). The mosdef survey: Measurements of balmer decrements and the dust attenuation curve at redshifts z 1.4–2.6*. *The Astrophysical Journal*, 806(2):259.

Reddy, N. A., Pettini, M., Steidel, C. C., Shapley, A. E., Erb, D. K., and Law, D. R. (2012). The characteristic star formation histories of galaxies at redshifts z 2–7*. *The Astrophysical Journal*, 754(1):25.

Reddy, N. A. and Steidel, C. C. (2004). X-ray and radio emission from ultraviolet-selected star-forming galaxies at redshifts 1.5 z 3.0 in the goods-north field*. *The Astrophysical Journal*, 603(1):L13.

Rémy-Ruyer, A., Madden, S. C., Galliano, F., Galametz, M., Takeuchi, T. T., Asano, R. S., Zhukovska, S., Lebouteiller, V., Cormier, D., Jones, A., Bocchio, M., Baes, M., Bendo, G. J., Boquien, M., Boselli, A., DeLooze, I., Doublier-Pritchard, V., Hughes, T., Karczewski, O. Ł., and Spinoglio, L. (2014). Gas-to-dust mass ratios in local galaxies over a 2 dex metallicity range. *Astronomy Astrophysics*, 563:A31.

Salim, S., Boquien, M., and Lee, J. C. (2018). Dust attenuation curves in the local universe: Demographics and new laws for star-forming galaxies and high-redshift analogs. *The Astrophysical Journal*, 859(1):11.

Salim, S. and Narayanan, D. (2020). The dust attenuation law in galaxies. *Annual Review of Astronomy and Astrophysics*, 58(1):529–575.

Scholtz, Jan, Maiolino, Roberto, D'Eugenio, Francesco, Curtis-Lake, Emma, Carniani, Stefano, Charlot, Stephane, Curti, Mirko, Silcock, Maddie S., Arribas, Santiago, Baker, William, Bhatawdekar, Rachana, Boyett, Kristan, Bunker, Andrew J., Chevallard, Jacopo, Circosta, Chiara, Eisenstein, Daniel J., Hainline, Kevin, Hausen, Ryan, Ji, Xihan, Ji, Zhiyuan, Johnson, Benjamin D., Kumari, Nimisha, Looser, Tobias J., Lyu, Jianwei, Maseda, Michael V., Parlanti, Eleonora, Perna, Michele, Rieke, Marcia, Robertson, Brant, Del Pino, Bruno Rodríguez, Sun, Fengwu, Tacchella, Sandro, Übler, Hannah, Venturi, Giacomo, Williams, Christina C., Willmer, Christopher N. A., Willott, Chris, and Witstok, Joris (2025). Jades: A large population of obscured, narrow-line active galactic nuclei at high redshift. *Astronomy Astrophysics*, 697:A175.

Shivaei, I., Reddy, N., Rieke, G., Shapley, A., Kriek, M., Battisti, A., Mobasher, B., Sanders, R., Fetherolf, T., Azadi, M., Coil, A. L., Freeman, W. R., de Groot, L., Leung, G., Price, S. H., Siana, B., and Zick, T. (2020). The MOSDEF Survey: The Variation of the Dust Attenuation Curve with Metallicity. *The Astrophysical Journal*, 899(2):117.

Shivaei, I., Reddy, N. A., Steidel, C. C., and Shapley, A. E. (2015). Investigating h, uv, and ir star-formation rate diagnostics for a large sample of z 2 galaxies. *The Astrophysical Journal*, 804(2):149.

Sommovigo, L., Cochrane, R. K., Somerville, R. S., Hayward, C. C., Lovell, C. C., Starkenburg, T., Popping, G., Iyer, K., Gabrielpillai, A., Ho, M., Steinwandel, U. P., and Perez, L. A. (2025). Learning the universe: physically-motivated priors for dust attenuation curves.

Wild, V., Charlot, S., Brinchmann, J., Heckman, T., Vince, O., Pacifici, C., and Chevallard, J. (2011). Empirical determination of the shape of dust attenuation curves in star-forming galaxies. *Monthly Notices of the Royal Astronomical Society*, 417(3):1760–1786.

Wu, J., Wu, Q., Xue, H., Lei, W., and Lyu, B. (2023). Steep balmer decrement in weak agns may not be caused by dust extinction: Clues from low-luminosity agns and changing-look agns. *The Astrophysical Journal*, 950(2):106.

Wuyts, S., Förster Schreiber, N. M., van der Wel, A., Magnelli, B., Guo, Y., Genzel, R., Lutz, D., Aussel, H., Barro, G., Berta, S., Cava, A., Graciá-Carpio, J., Hathi, N. P., Huang, K.-H., Kocevski, D. D., Koekemoer, A. M., Lee, K.-S., Le Floc'h, E., McGrath, E. J., Nordon, R., Popesso, P., Pozzi, F., Riguccini, L., Rodighiero, G., Saintonge, A., and Tacconi, L. (2011). Galaxy Structure and Mode of Star Formation in the SFR-Mass Plane from z ~2.5 to z ~0.1. *The Astrophysical Journal*, 742(2):96.